Journal of
Instrumentation

PAPER • OPEN ACCESS

Project 8 apparatus for cyclotron radiation emission spectroscopy with ^{83m}Kr and tritium

To cite this article: A. Ashtari Esfahani *et al* 2026 *JINST* **21** P02026

Published by IOP Publishing for Sissa Medialab
Received: *March 20, 2025*
Revised: *July 10, 2025*
Accepted: *September 2, 2025*
Published: *February 12, 2026*

Project 8 apparatus for cyclotron radiation emission spectroscopy with ^{83m}Kr and tritium

PROJECT 8

The Project 8 collaboration

A. Ashtari Esfahani[a,*] **D.M. Asner**[b] **S. Böser**[c] **N. Buzinsky**[d] **R. Cervantes**[a] **C. Claessens**[a,c] **L. de Viveiros**[e] **P.J. Doe**[a] **J.L. Fernandes**[b] **M. Fertl**[c] **J.A. Formaggio**[d] **D. Furse**[d] **L. Gladstone**[f] **M. Guigue**[g] **J. Hartse**[a] **K.M. Heeger**[h] **X. Huyan**[b] **A.M. Jones**[b] **J.A. Kofron**[a] **B.H. LaRoque**[b] **A. Lindman**[c] **E. Machado**[a] **E.L. McBride**[a] **P. Mohanmurthy**[d] **R. Mohiuddin**[f] **B. Monreal**[f] **E.C. Morrison**[b] **J.A. Nikkel**[h] **E. Novitski**[a] **N.S. Oblath**[b] **M. Ottiger**[a] **W. Pettus**[i] **R. Reimann**[c] **R.G.H. Robertson**[a] **G. Rybka**[a] **D. Rysewyk**[d] **L. Saldaña**[h] **P.L. Slocum**[h] **M.G. Sternberg**[a] **Y.-H. Sun**[f] **P.T. Surukuchi**[h,j] **J.R. Tedeschi**[b] **A.B. Telles**[h] **F. Thomas**[c] **M. Thomas**[b] **T. Thümmler**[k] **L. Tvrznikova**[l] **B.A. VanDevender**[b] **M. Wachtendonk**[a] **M. Walter**[k] **J. Weintroub**[m] **T.E. Weiss**[d,h] **T. Wendler**[e] **N.L. Woods**[a] **E. Zayas**[d] **and A. Ziegler**[e]

[a] *Center for Experimental Nuclear Physics and Astrophysics and Department of Physics, University of Washington, Seattle, WA 98195, U.S.A.*
[b] *Pacific Northwest National Laboratory, Richland, WA 99354, U.S.A.*
[c] *Institute for Physics, Johannes Gutenberg University Mainz, 55128 Mainz, Germany*
[d] *Laboratory for Nuclear Science, Massachusetts Institute of Technology, Cambridge, MA 02139, U.S.A.*
[e] *Department of Physics, Pennsylvania State University, University Park, PA 16802, U.S.A.*
[f] *Department of Physics, Case Western Reserve University, Cleveland, OH 44106, U.S.A.*
[g] *Laboratoire de Physique Nucléaire et de Hautes Energies (LPNHE), Sorbonne Université, Université Paris Diderot, CNRS/IN2P3, 75005 Paris, France*
[h] *Wright Laboratory, Department of Physics, Yale University, New Haven, CT 06520, U.S.A.*
[i] *Center for Exploration of Energy and Matter and Department of Physics, Indiana University, Bloomington, IN, 47405, U.S.A.*
[j] *Department of Physics & Astronomy, University of Pittsburgh, Pittsburgh, PA 15260, U.S.A.*
[k] *Institute for Astroparticle Physics, Karlsruhe Institute of Technology, 76021 Karlsruhe, Germany*
[l] *Lawrence Livermore National Laboratory, Livermore, CA 94550, U.S.A.*
[m] *Center for Astrophysics | Harvard & Smithsonian, Cambridge, MA 02138, U.S.A.*

E-mail: ashtari@uw.edu

[*] Corresponding author.

https://doi.org/10.1088/1748-0221/21/02/P02026

2026 JINST 21 P02026

Abstract: Cyclotron Radiation Emission Spectroscopy (CRES) is a novel technique for the precise measurement of relativistic electron energy. This technique is being employed by the Project 8 collaboration for measuring a high-precision tritium beta decay spectrum to perform a frequency-based measurement of the neutrino mass. In this work, we describe the Project 8 Phase II apparatus, used for the detection of the CRES signal from the conversion electrons of ^{83m}Kr and the first CRES measurement of the beta-decay spectrum of molecular tritium.

Keywords: Neutrino detectors; Spectrometers

ArXiv ePrint: 2503.08807

2026 JINST 21 P02026

Contents

2026 JINST 21 P02026

1 Introduction

The observation of neutrino flavor transformation proved that neutrinos have non-zero mass [1, 2], a result that contradicts the expectation from the Standard Model of Particle Physics. However, the absolute mass scale of these fundamental fermions remains unknown [3].

Various techniques are being used in the ongoing quest to measure neutrino mass. If neutrinos are Majorana particles, their mass can be measured in the laboratory by searching for neutrinoless double-beta decay [4–9]. Cosmological measurements of large-scale structure, interpreted in the ΛCDM model framework, offer another indication of the neutrino mass scale, albeit with significant model-dependence [10–12].

The kinematics of beta decay [13, 14] and electron capture [15, 16] are affected by finite neutrino masses that cause distortions of the decay spectrum which provide direct and model-independent access to the neutrino masses, independently of their Dirac or Majorana nature [17, 18]. When the masses are not resolved, these experiments are sensitive to an electron-weighted neutrino mass

$$m_\beta = \sqrt{\sum_{i=1}^{3} |U_{ei}|^2 m_i^2}, \tag{1.1}$$

where U_{ei} are elements of the Pontecorvo-Maki-Nakagawa-Sakata matrix and m_i are neutrino mass eigenvalues [19, 20].

The current state-of-the-art direct neutrino mass experiment is KATRIN, which has an ultimate sensitivity goal to a (anti)neutrino mass of 300 meV/c^2 (90% C.L.) [13, 21]. KATRIN measures the beta-decay spectrum of molecular tritium, whose shape near the endpoint is modified by the neutrino mass. However, investigating the mass range below 100 meV/c^2 with tritium is only practically possible in atomic form to avoid the energy broadening caused by the rovibrational initial and final states of the molecules [18, 22, 23]. Extending the neutrino mass reach of beta-decay experiments also requires excellent energy resolution, low background, high statistics, and careful control of systematic effects.

The Project 8 collaboration has pioneered the Cyclotron Radiation Emission Spectroscopy (CRES) technique, targeting a next-generation direct (anti)neutrino mass sensitivity of 40 meV/c^2 using tritium beta decay. This technique measures the kinetic energy of an electron via the frequency of the cyclotron radiation it emits while undergoing cyclotron motion in a magnetic field. The cyclotron frequency is

$$f_c = \frac{f_0}{\gamma} = \frac{1}{2\pi}\frac{|e|B}{m_e + K_e/c^2}, \tag{1.2}$$

where f_0 is the non-relativistic cyclotron frequency, $\gamma = 1 + K_e/m_e c^2$ is the Lorentz factor, B is the magnetic field, and e, m_e, and K_e are the electron's charge, mass, and kinetic energy [24]. While neutrino mass measurement is a primary application of Cyclotron Radiation Emission Spectroscopy, it is also used to measure highly relativistic electron and positron energies from ^{6}He and ^{19}Ne beta decays, opening a new avenue for searches for signatures of beyond Standard Model physics through precision beta-decay measurements [25, 26]. There is also a proposal to utilize CRES for ultra-high resolution X-ray spectroscopy [27].

CRES data can be fast-Fourier-transformed and represented as a spectrogram, as shown in figure 1. "Tracks" of higher radiated power, originating from beta-electron cyclotron radiation, stand out above the thermal noise. As an electron emits cyclotron radiation, its energy decreases, leading to a gradual increase in its cyclotron frequency (eq. (1.2)) and causing the upward slopes of the tracks. The abrupt frequency jumps are caused by energy loss due to collisions of the electron with residual gas molecules in the CRES cell. The electron tracks are detected and grouped to reconstruct individual electron events [28]. For each reconstructed event, the electron's start frequency is deduced, which is then used to determine the electron's initial energy before it had lost energy to radiation or scattering.

The Project 8 collaboration plans to reach its design sensitivity to neutrino mass as the conclusion of a program in four phases [29, 30]. Phase I demonstrated CRES in a small active volume using a rectangular waveguide to collect the cyclotron radiation from mono-energetic conversion electrons emitted by metastable krypton atoms (^{83m}Kr) [31]. In Phase II, described here, the first tritium spectrum was measured in an upgraded but still-small (O(cm^3)) circular-waveguide-based apparatus, using the same magnet. This measurement resulted in the extraction of the first frequency-based neutrino mass limit of $m_\beta < 155\,\mathrm{eV}/c^2$ (152 eV/c^2) in a Bayesian (frequentist) analysis [14, 32]. Phase III will demonstrate the key technologies for a full-scale measurement: the production and trapping of cold atomic tritium, and CRES in large (O(m^3)) volumes using a resonant cavity detector with higher efficiency and improved resolution. The final Phase IV will scale to reach the ultimate neutrino mass sensitivity goal of 40 meV/c^2 [33].

Hardware innovations were key to enabling the accomplishments of Phase II. The first CRES-based neutrino mass limit was made possible by a tritium-compatible gas handling system. Crucially, new hardware also enabled the control and precise characterization of the Phase II apparatus, enabling the demonstration of CRES's potential as a precision measurement technique [14, 32]. Thermal RF noise

2026 JINST 21 P02026

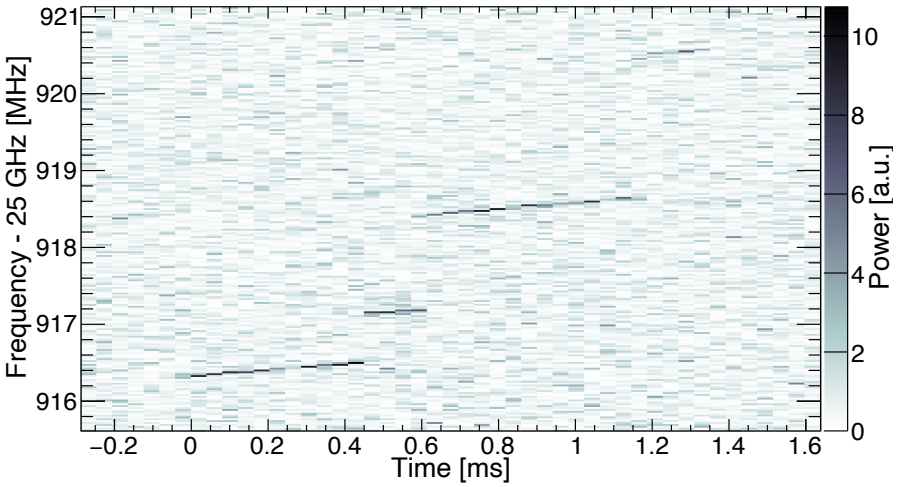

Figure 1. Spectrogram of a CRES event from an electron emitted in tritium decay, detected with the Phase II apparatus. Raw time-series data are Fourier transformed in time bins of 40.96 µs, yielding 24.41 kHz frequency bins. Reproduced from [14]. CC BY 4.0.

was the primary source of background, the control of which enabled a measurement with zero counts above the tritium endpoint in the 82-day data-taking period. A new field-shifting solenoid made it possible to map the relationship of detection efficiency with signal frequency, allowing for the control of related uncertainties. Better magnetic field characterization and magnetic trap control enabled an improved understanding of the contributions of magnetic field inhomogeneities to detector response, while a new gas system with precise gas density control and gas composition characterization provided insight into scattering-related effects on detector response. These together led to a demonstrated resolution of 1.66 eV FWHM. In this work, we describe the design and characterization of the apparatus (figure 2) that enabled the advances in Phase II of Project 8 [34].

In this Phase II experiment, the cyclotron frequency is 25.9 GHz for the highest-energy electrons in the tritium spectrum in a 0.959 T magnetic field. A Nuclear Magnetic Resonance (NMR) magnet was used to produce the field (section 2). A cryogenic insert positions the CRES cell, a waveguide section where the decay electrons are produced and measured, at the maximum of the magnetic field. The insert also supports the cyclotron radiation transfer to the amplifiers, the radioactive gas connection, and the coils to generate the magnetic field for electron trapping (section 3). After amplification, a room-temperature receiver system filtered, down-converted, and digitized the signal (section 4). The last essential part of the Phase II apparatus was the gas delivery system, which was designed to provide the proper composition and pressure of the radioactive gases (section 5).

2 Magnet

A warm-bore Bruker-Spectrospin 200 MHz superconducting NbTi NMR magnet (figure 2) produced the 0.959 T magnetic field of the experiment. The magnetic field was pointed upwards, towards the amplifiers, resulting in left-handed circularly polarized radiation.

A non-functional trim coil limited the magnetic field homogeneity, but the 20 ppm homogeneity achieved across the 25 mm diameter with the seven working shim coils was sufficient for Phase II of Project 8 [35, 36]. Figure 3 shows an on-axis magnetic field strength measurement with a Metrolab

2026 JINST 21 P02026

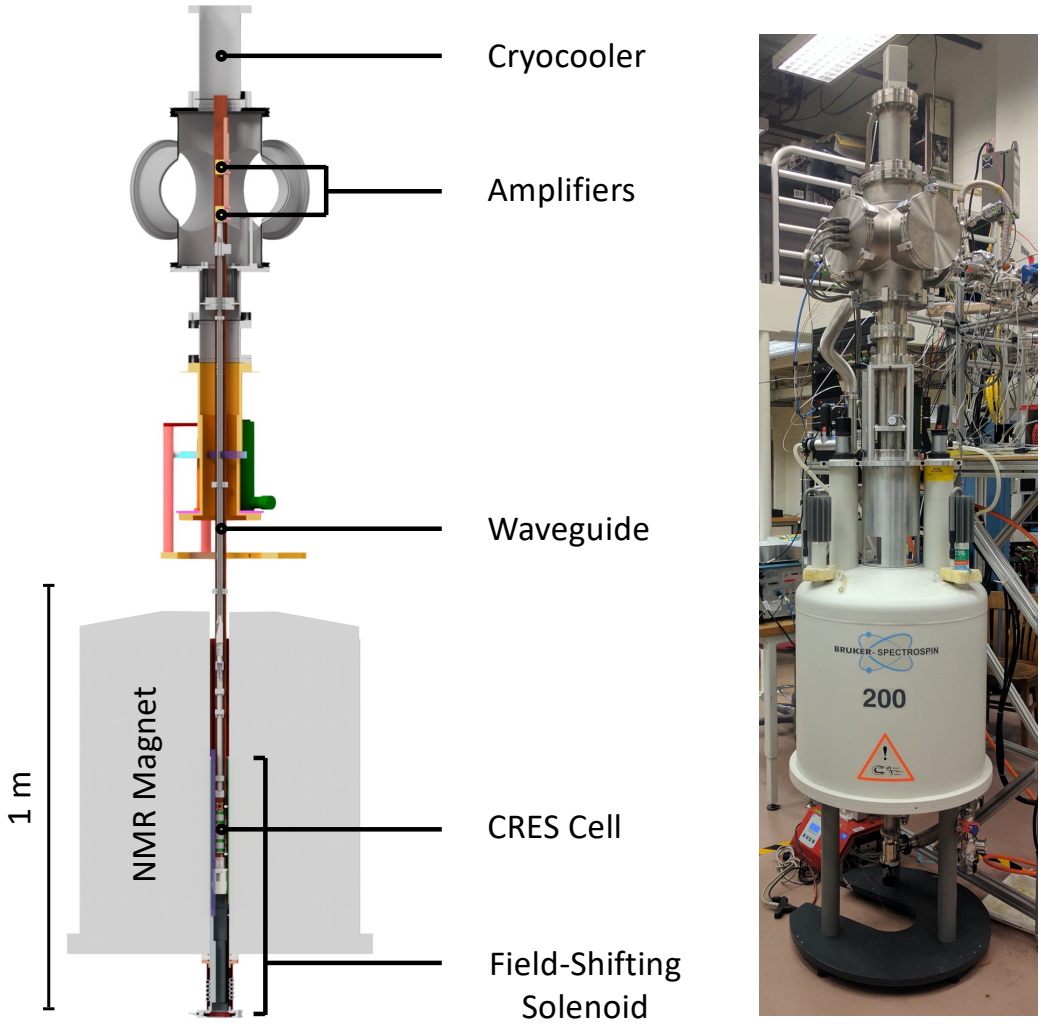

Figure 2. A model cross-section (left) and photograph (right) of the apparatus used in Phase II of the Project 8 experiment. The superconducting NMR magnet is visible at the center. The CRES cell was supported by a cryogenic insert, suspended inside the field-shifting solenoid within the magnet's bore. Two cryogenic amplifiers attached to the cryocooler fixed the signal to noise ratio of the entire signal chain.

PT2025 NMR teslameter, alongside four additional measurements taken at 12.5 mm radial offsets in different azimuthal positions. The radial inhomogeneity in the background magnetic field, while less pronounced than the variation from the trapping coils, degrades the energy resolution. A Pfeiffer HiCube 80 turbomolecular pump was used to keep the pressure in the bore below 10 µtorr. The CRES cell outer vacuum system was connected to the magnet bore by a sliding piston seal and could be raised and lowered by means of a hydraulic cylinder. The CRES cell vertical position in the background field was adjusted to maximize field homogeneity across the electron trapping volume. The desired vertical position was then fixed with machined aluminum blocks.

A non-superconducting solenoid, called the field-shifting solenoid, was installed inside the NMR magnet's bore to alter the magnetic field at the location of the CRES cell for systematic studies (figure 4) [32, 37]. The background field was shifted to vary the cyclotron frequency of 17.824 keV mono-energetic conversion electrons from ^{83m}Kr to investigate the frequency-dependent features of

2026 JINST 21 P02026

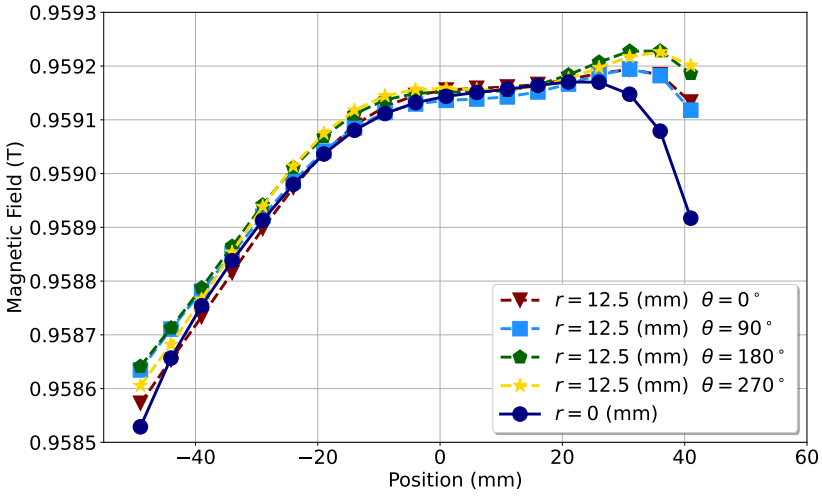

Figure 3. The magnetic field measurements at the center of the magnet bore on the axis of the magnet and at $r = 12.5$ mm in four azimuthal positions, performed in April 2018 [35]. The insert's axial position corresponds with the choice where the physics data was recorded. The zero of the axial position is at the center of the central trap coil.

the signal. Two layers of AWG26 copper magnet wire potted in varnish were wound onto a 1.4 mm thick copper cylinder that fit around the cryogenic insert, within the NMR magnet. The coil form was brazed to a bolted O-ring flange that mated to the bottom of the NMR magnet, below which were brazed five rounds of copper tubing for cooling water. A 1 A current generated a 4.9 mT field, which was sufficient to shift the cyclotron frequency of the 17.824 keV electrons by ∼130 MHz. Using COMSOL simulation software, the spatial variation along the CRES cell's length in the field created by the field-shifting solenoid was estimated to be less than 40 µT.

The temperature of the CRES cell was initially stable with the field-shifting solenoid installed, but later became unstable due to the development of a poorly-understood thermal link. Since the frequency-dependent systematic studies had already been concluded by then, the solenoid was removed before proceeding with the tritium data campaign in Phase II.

3 Cryogenic insert

Both the CRES cell and the amplifiers needed to be held at cryogenic temperatures to reduce the thermal RF noise that causes the background in figure 1. The CRES cell, the RF power transfer section, and the amplifier stage comprised the cryogenic insert (figure 5). A 2.5 cm × 1 cm copper bar was the mechanical backbone for the cryogenic insert. The copper bar and the amplifiers were connected in parallel to a Cryomech AL60 single-stage Gifford-McMahon cryocooler using copper braids. This group of components was held at low temperatures to minimize the addition of thermal noise before the amplification of the CRES signal. The amplifiers were at ∼ 30 K, while the CRES cell temperature was raised to 85 K using a software PID (proportional-integral-differential) loop-stabilized heater to prevent the ^{83m}Kr from freezing to the CRES cell walls. This temperature was experimentally optimized to maximize the recorded event rate [32].

2026 JINST 21 P02026

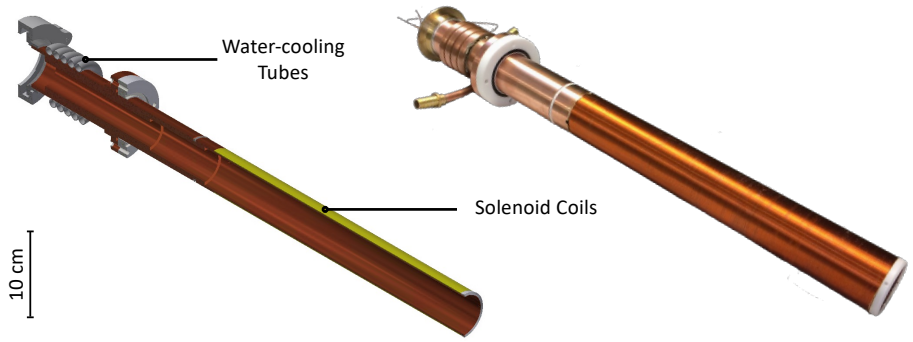

Figure 4. A model cross-section (left) and photo (right) of the field-shifting solenoid used in Phase II of the experiment. The solenoid was 350 mm long with an outer diameter of 52 mm and an inner diameter of 46 mm. It was used to homogeneously shift the background magnetic field to vary the cyclotron frequency of mono-energetic electrons from ^{83m}Kr for studying frequency-dependent systematic effects.

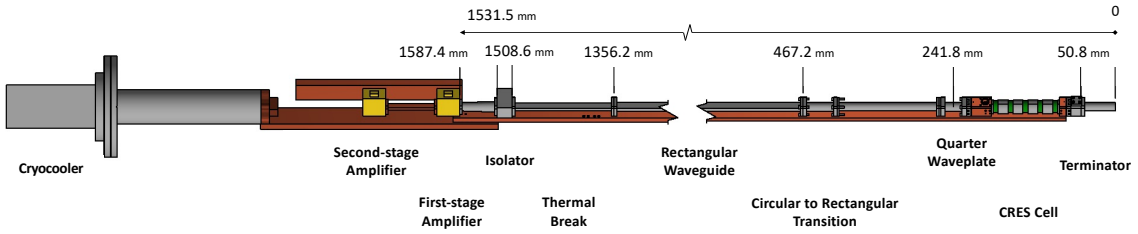

Figure 5. Cryogenic insert. The CRES cell is shown on the right side of the picture. Multiple components of the RF power transfer section are apparent (see section 3.4). The cryocooler is connected to the cryogenic insert on the left side of the picture.

3.1 CRES Cell

The CRES cell (figure 6) was designed to be an efficient microwave guide for the frequency range of interest. Furthermore, the cell had to be able to confine the radioactive gas while disturbing the waveguide's RF properties as little as possible. Therefore, two microwave-transparent windows were installed into the waveguide structure.

Two 2.4 mm thick pieces of CaF_2 were selected for the construction of the windows. This length corresponds to half a wavelength at 24.5 GHz.[1] RF simulations confirmed the windows' transparency in the frequency region of interest. Furthermore, the similarity of the thermal expansion coefficients of CaF_2 and copper ensured a safe cooldown where the vacuum integrity of the CRES cell was preserved to avoid a tritium leak [39]. Laser-cut indium gaskets were used to make the vacuum seal between the windows and the cylindrical cell wall. Titanium and aluminum bolts sustained mechanical pressure over the entire range from room temperature to 50 K, preserving vacuum integrity.

After installing the CaF_2 windows, the RF transmission properties of the CRES cell were measured with a network analyzer. The results shown in figure 7 confirmed a 1.7 GHz wide frequency window with ≤ 0.5 dB attenuation. However, not all of the bandwidth was available, as the signal was down-converted by 24.5 GHz (section 4).

[1] CaF_2 has a relative permittivity of 6.5 at temperatures lower than 100 K [38].

2026 JINST 21 P02026

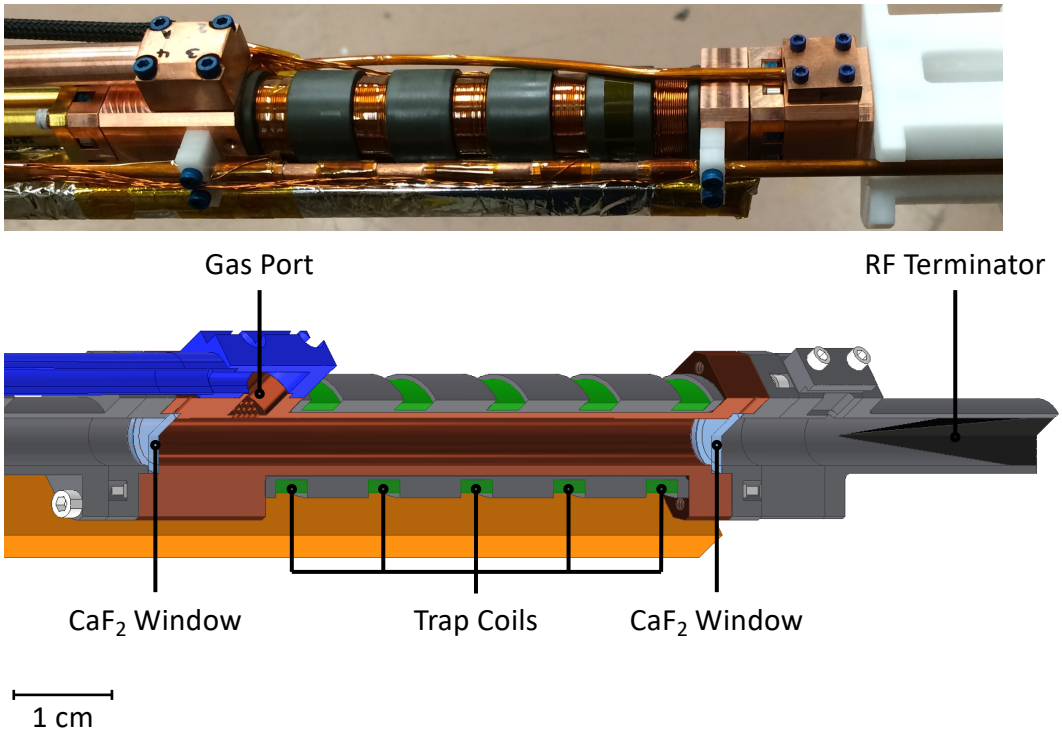

Figure 6. The CRES cell used in Phase II of the experiment (top) and its schematic diagram (bottom). Five trapping coils were available to generate the desired magnetic trapping geometry. A Torlon support structure connected the traps, thermally and mechanically, to the CRES cell. Two CaF_2 windows confined the radioactive gas inside the cell. Radioactive gases were admitted through a dedicated gas port. The conical terminator, manufactured with epoxy and graphite, was used to reduce the effects of interference.

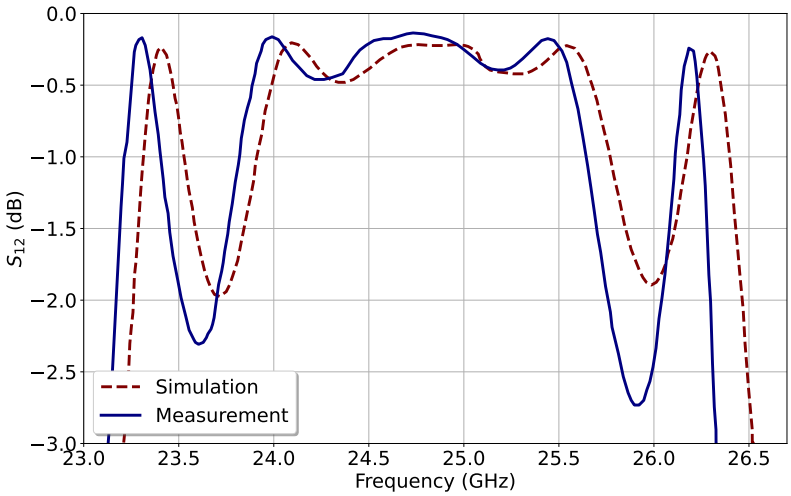

Figure 7. Simulated and measured transmission performance for the entire CRES cell assembly with CaF_2 windows installed at room temperature. The 0.4% frequency shift is attributed to differences in the CaF_2 window thickness and dielectric constant in simulation vs. assembled cell. Transmission changes stemmed primarily from RF reflections off the windows. Such frequency-dependent effects were corrected based on the systematic studies of the entire receiver system's efficiency using the field-shifting solenoid [32].

3.2 Magnetic trap

The strong homogeneous magnetic field that causes cyclotron motion confines electrons radially. However, without axial confinement, relativistic electrons would escape the observation region in a fraction of a microsecond, making it impossible to detect the CRES signal over noise. A magnetic bottle was used for axial electron trapping. Magnetic bottles, also called magnetic mirrors, confine electrons using only a magnetic field gradient. In the adiabatic limit, an electron's magnetic moment is a constant of motion, so the "pitch angle"—the angle of the electron's motion with respect to the magnetic field—shifts as the field strength changes. In a magnetic bottle, electrons in a certain range of momenta reach a pitch angle of 90°, turn around, experience the same on the other side, and are trapped. A detailed description of magnetic bottles' use to trap electrons for CRES is in [40], and a detailed analysis of the effects of the small magnetic field inhomogeneities on CRES signals is in [32].

To produce the magnetic bottle field for electron confinement, coils made of AWG 26 copper wire were wound around the microwave guide on a Torlon support structure (figure 6). The high thermal conductivity of Torlon enabled sufficient cooling for coils operating at 1 A. The coils were also potted in GE varnish 7031 to facilitate heat transfer out of the coils. Five trap coils were installed to make it possible to test multiple trap configurations. Individual coils could be used to create small dips in the field, each serving as its own trap. Alternatively, long "bathtub" traps of varying lengths could be created by running a pair of coils to produce a bump in the field at each end. In the end, bathtub traps suffered from a too-high modulation index (see ref. [40] for more detail), spreading RF power across too many sidebands and weakening the main carrier CRES signal. Therefore, combinations of near-harmonic individual dip traps, each with modulation index near 1, were used for almost all Phase II data. Another advantage of using multiple individual harmonic traps was that their strengths could be tuned individually to match the different traps' central magnetic fields to each other, and therefore to match cyclotron frequency distributions of trapped electrons.

Two different trap configurations were used in Phase II. First, to establish the high-resolution capabilities of the CRES technique, a "shallow trap" configuration with two trap coils was used with small currents (12.00 mA and 17.85 mA, supplied by two Stanford Research Systems LDC 501 precision power supplies) to minimize the systematic effects caused by the magnetic field variation experienced by the trapped electrons (figure 8). Second, for acquiring data at higher event rates, a "deep trap" configuration with four field dips (174 mA, 249 mA, 272 mA, and 286 mA, with the additional currents supplied by an AIM-TTI MX100TP power supply) was used. The deep-trap configuration increased the event rate by a factor of 40 at the expense of a factor-of-30 worsening in the energy resolution. The fifth coil was not used in this configuration as it was sited in the steep region of the background field, making it so that no equivalent-depth field minimum could be formed. Only the deep-trap configuration was used for the tritium spectrum measurement because the neutrino mass uncertainty was statistics-limited, whereas both shallow- and deep-trap configurations were used for krypton measurements [14, 32].

3.3 Waveguide design

The waveguide design in Project 8 was optimized for electron energies in the range of 10 to 32 keV. These electrons radiate power in the microwave K-band frequency range in the presence of the 0.959 T magnetic field. A segment of a K-band circular waveguide, with an inner diameter of 10 mm (0.396"),

2026 JINST 21 P02026

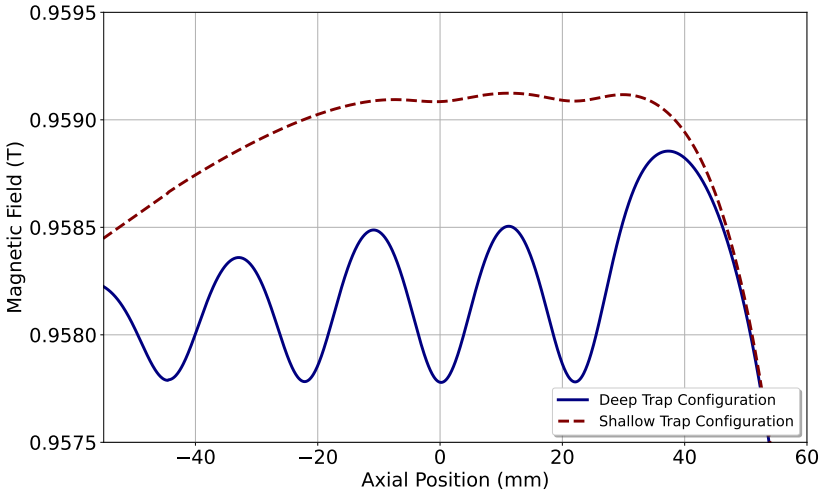

Figure 8. The magnetic field of four traps in the deep trap configuration and two traps in the shallow trap configuration, the two common trap configurations used in Phase II. The overall shape of the field is formed by the background field (figure 3), while the local minima are generated by the magnetic field of the traps.

was used as the CRES cell in Phase II of the experiment.[2] Electrons' cyclotron motion couples to the first two modes of the circular waveguide, TE_{11} and TM_{01}. The symmetry of a cylindrical waveguide with perpendicular electric field components in its fundamental mode (TE_{11}) provides a more efficient coupling to the cyclotron electron compared with the fundamental mode of a rectangular waveguide (TE_{10}) used in Phase I of the experiment. Figure 9 compares the power radiated into the fundamental modes for electrons in the circular CRES cell used in Phase II with that for the rectangular waveguide used in Phase I. With its larger cross-section, the circular waveguide also had a larger physical volume and therefore higher radioactivity in the cell at a given pressure and temperature. The choice of copper for the CRES cell limited the attenuation due to the resistive losses in the waveguide walls to be less than $0.25\,\mathrm{dB\,m^{-1}}$ in the frequency range of interest. Figure 6 shows the CRES cell for Phase II. The gas port connection to the CRES cell was through a grid of sub-wavelength holes, which did not degrade RF transmission along the signal path.

3.4 RF power transfer and amplification

The RF power transfer section of the apparatus was designed to allow the microwave radiation to propagate from the electron in the CRES cell to the cryogenic amplifiers (figure 5). This section's length was defined by the need to locate the isolator and the two low-noise amplifiers outside the strong magnetic field region.

After leaving the CRES cell, circularly polarized radiation was converted to linear polarization in a QuinStar MN: QWL-26MKFOZ396 left-circular polarization quarter-wave plate. Next, a circular-to-rectangular waveguide adapter transitioned the electromagnetic radiation into the 0.9 m long copper WR-42 waveguide, which carried the radiation out of the strong field region.

[2]Increasing the volume of the electron trapping region would have increased the number of radioactive gas molecules and the number of decays observed. However, increasing the cross-sectional dimensions could have induced coupling of the electrons to non-fundamental modes in the waveguide, increasing the complexity of data analysis.

2026 JINST 21 P02026

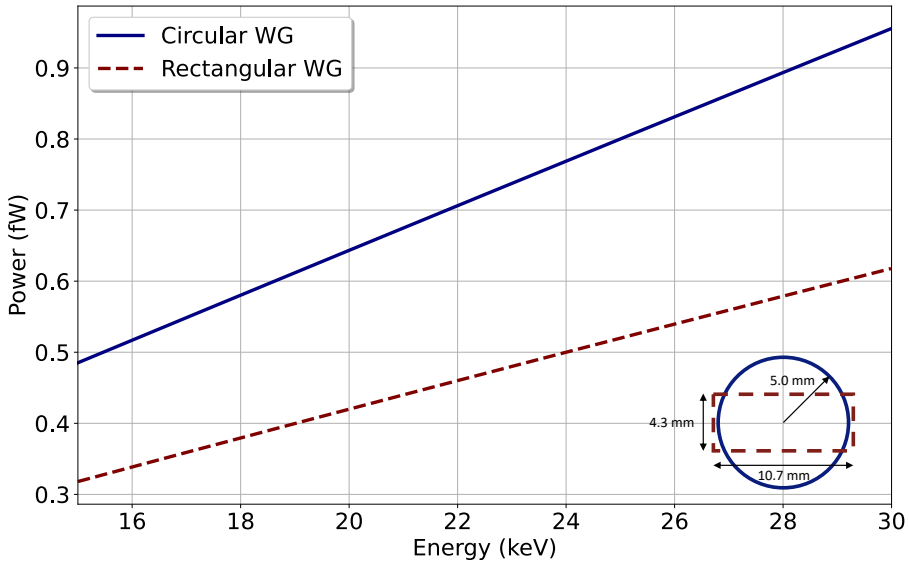

Figure 9. Electron radiated power into the fundamental modes of the circular waveguide used in Phase II and the WR-42 rectangular waveguide used in Phase I of the experiment, as a function of electron energy. The calculation is based on the phenomenological model developed in [40]. The cross-sections of the waveguides are shown in the lower right corner.

To prevent the heat from the 85 K region from warming the amplifiers (which would have raised the noise temperature), a low-thermal-conductivity but also low-RF-loss gold-coated stainless steel section of WR-42 waveguide, 152 mm long, was added following the long copper WR-42 waveguide. Figure 10 shows the temperature profile along the insert during a system cool-down, demonstrating the effectiveness of the thermal break in isolating the temperature of the amplifiers and isolator from the CRES cell. A Raditek RADI-18-26.5-Cryo-(4-77K)-WR42 RF isolator (a circulator with one port terminated) then terminated any power reflected from the amplifiers and flattened the frequency dependence of the gain and noise (figure 11). Finally, a waveguide taper transitioned to the WR-28 input port of the first of a cascaded pair of 28 dB gain Low Noise Factory LNF-LNC22-40WA amplifiers, which were connected by a section of gold-coated WR-28 waveguide.

3.5 Waveguide terminator

One significant change between Phase I and Phase II was how CRES radiation that was originally propagating downward, away from the amplifiers, was handled. In Phase I, a reflecting RF short at the lower end of the waveguide reflected this initially-downward-propagating CRES radiation upward and to eventually be detected. Although this increased the maximum signal amplitude, destructive interference of the reflected and the propagated waves generated frequency and position-dependent signal features. This effect is visible in the Phase I event with a missing main carrier in figure 1 of ref. [41], and there is discussion of the phenomenology in this case in section VI of ref. [40]. In contrast, in Phase II, an absorbing RF terminator at the bottom of the cell prevented these reflections, sacrificing some of the available signal power but consistently giving the clean morphology shown in figure 1. This also led to much more consistent detection efficiency across the frequency region of interest, a crucial feature for a tritium endpoint experiment.

2026 JINST 21 P02026

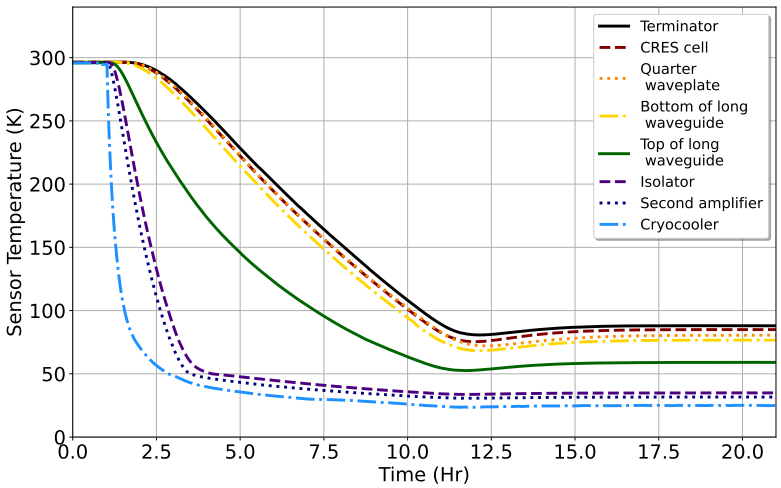

Figure 10. Temperature profile along the insert during a system cool-down. First, the temperature drops following cryocooler activation. Then, the CRES cell heater is activated to raise and stabilize the CRES cell temperature to its 85 K operating temperature.

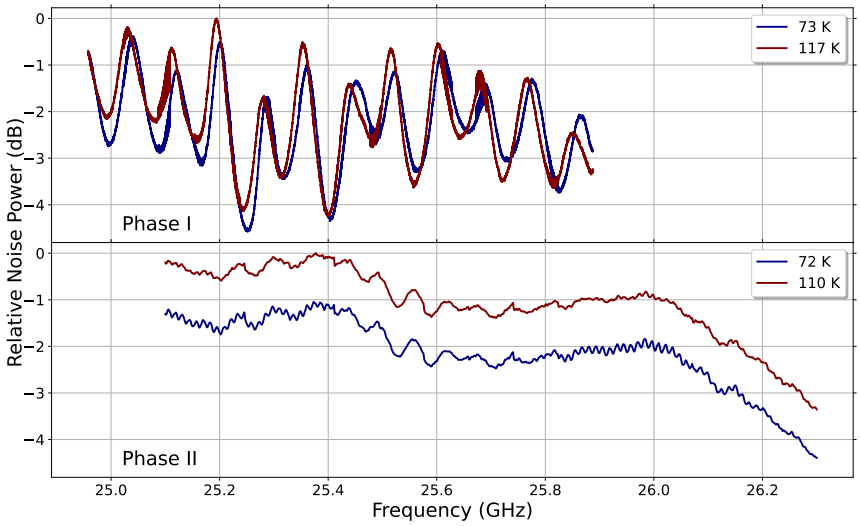

Figure 11. Comparison of measured RF noise power between Phase I and Phase II at different cell temperatures, as measured by the Tektronix Realtime Spectrum Analyzer (RSA). In contrast to the Phase II system, the Phase I insert had a reflecting short beyond the cell and did not include a circulator. The high-frequency stage was rebuilt between experimental phases (see section 4), changing the overall system gain so that only a relative comparison is possible. The complete characterization of the full system RF noise, with the production receiver configuration, is described in appendix A. The noise temperatures were determined to be 145 K [31] and 132 K in Phases I and II, respectively. The strong suppression in noise fluctuations is due to the addition of the circulator, which results in a flatter frequency response.

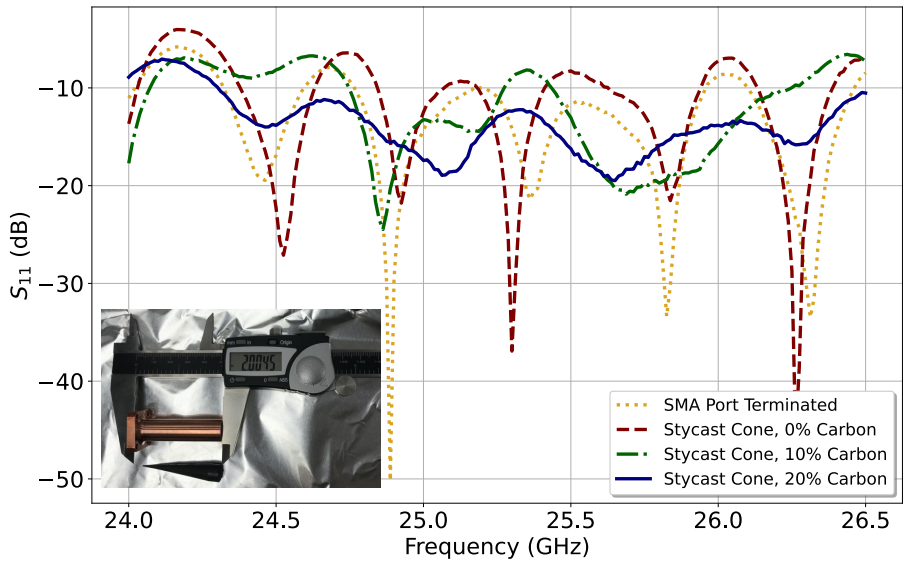

Figure 12. Measured reflection coefficients for the three locally fabricated epoxy/graphite terminators and for a commercial ANNE-50L+12 GHz SMA terminator. The commercial terminator was imperfect in this frequency range because it was designed for 12 GHz. Ultimately, the terminator with 20% carbon was used. The epoxy/graphite cone and waveguide housing that made up the terminator are shown at the bottom left.

Commercial cryogenic RF terminators were not available in the required geometry, so a terminator was fabricated locally. It was cast from a non-magnetic and RF-dissipative mixture of Stycast 1266 epoxy and superfine natural graphite spherical powder. A conical design was chosen to provide a gradual change in impedance that maximally suppressed reflections.

Three terminators with 0%, 10%, and 20% graphite concentration by weight were cast and characterized. Figure 12 shows the reflection coefficients of these terminators compared to a commercial terminator. As expected, the lossiness induced by the graphite reduced the quality factors of resonant features. As the concentration of graphite was increased, these features widened in frequency and decreased in amplitude until the loss was sufficient to make them no longer distinct. The terminator with 20% graphite concentration was selected because its attenuation was the least frequency-dependent.

4 RF receiver system

After the cold signal amplification (see section 3.4), a series of room-temperature RF components were used to filter, downmix, amplify, digitize, and monitor the CRES signals (see figure 13). Here, these warm RF components are detailed, followed by the result of an analysis of the gain and the noise of the RF receiver chain. A common 10 MHz reference signal from a Stanford Research Systems FS725 rubidium clock was provided throughout the RF system.

The high-frequency mixing stage was designed to convert the raw RF signals down to intermediate frequency (IF) $\lesssim$ 2 GHz, suitable for digitization (see figure 14). The input signal was carried on a short coaxial cable from the vacuum space feed-through to this stage. The signal was first amplified by a low-noise Quinstar QLW-18262530-J0 amplifier before a Krytar 6180400K matched-line directional two-way power divider split the signal into two paths. Both signal paths used a Lorch

2026 JINST 21 P02026

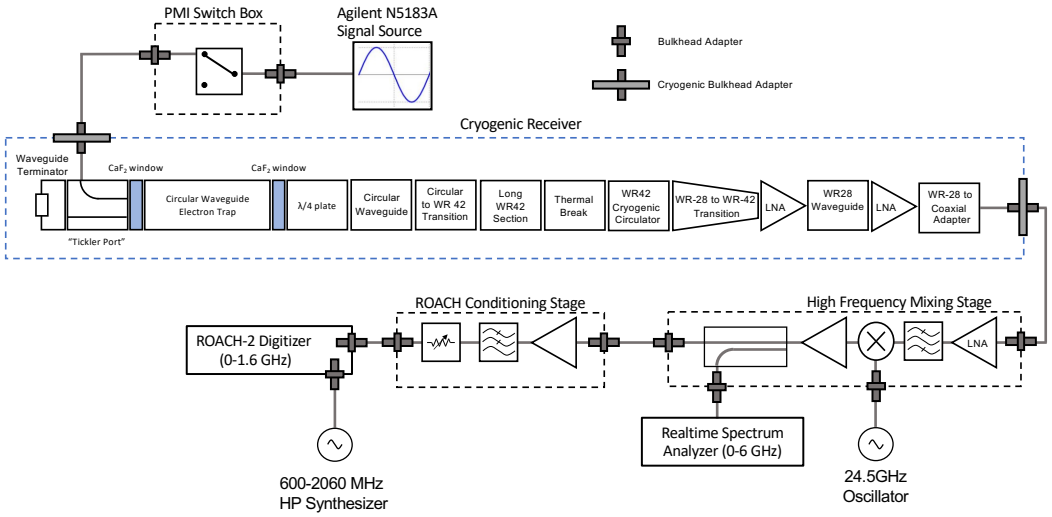

Figure 13. The Phase II RF receiver chain. The signal-to-noise ratio was fixed in the cryogenic receiver following the second low-noise amplifier. A high-frequency mixing stage bandpass filtered the signal and mixed down to intermediate frequency (IF). A second conditioning stage provided additional filtering and amplification. Two digitizer systems were available: primary physics data was collected with a ROACH-2 digitizer system, while a Realtime Spectrum Analyzer (RSA) was used for system commissioning and for validation. The high-frequency mixing stage and ROACH conditioning stage are expanded in greater detail in figures 14 and 15, respectively.

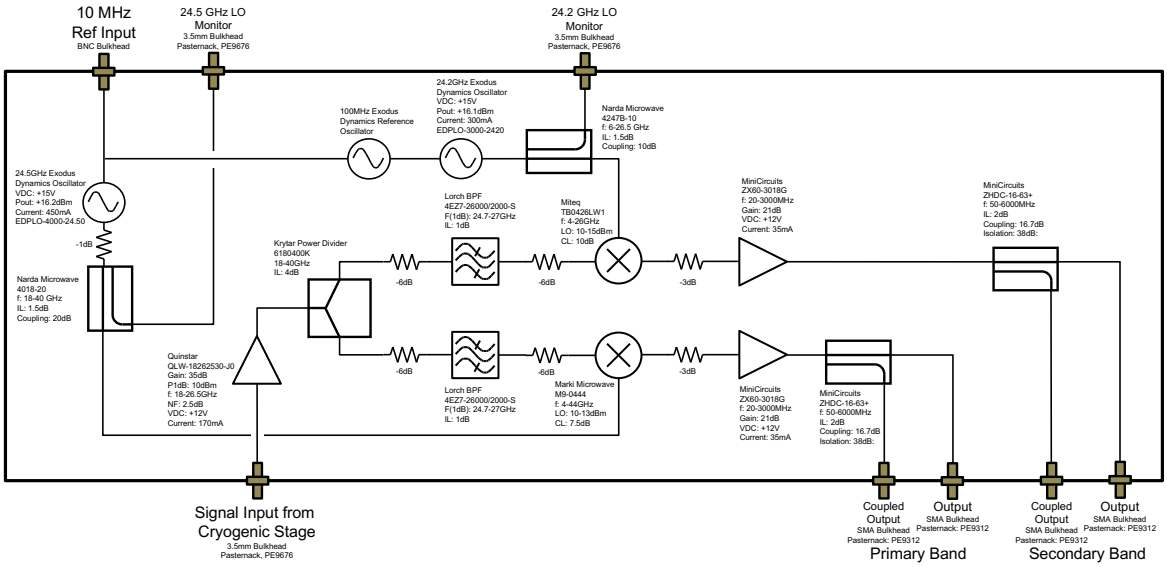

Figure 14. The Phase II high-frequency mixing stage. The ~26 GHz RF CRES signals were bandpass-filtered and downmixed to IF by 24.5 GHz for the primary band. The output and coupled outputs were connected to the ROACH conditioning stage and RSA, respectively.

4EZ7-26000/2000-S bandpass filter with a range 24.7–27.0 GHz to avoid image bandwidth noise when mixed. The primary signal path was downmixed with a 24.5 GHz reference from an Exodus Dynamics EDPLO-4000 phased-locked oscillator using a Marki Microwave M9-0444 double-balanced mixer. A secondary signal path was downmixed with a 24.2 GHz reference and comparable components. Attenuators and amplifiers along the RF path ensured the signal was maintained in the optimal range and noise was minimized. Directional couplers allowed for the monitoring of the oscillator signals or mixed signals from the high-frequency mixing stage in parallel with data taking.

System commissioning was performed with signals downmixed by the secondary 24.2 GHz oscillator, available from the Phase I receiver. These measurements determined 24.5 GHz to be the ideal reference, and the high-frequency stage was rebuilt as depicted to accommodate the parallel primary and secondary bands, allowing a direct crosscheck of performance with the commissioning setup. This reference choice provides full coverage of the tritium endpoint region within the Reconfigurable Open Architecture Computing Hardware-2 (ROACH-2) digitizer [42] sampling bandwidth, placing the tritium endpoint (18.574 keV) at 1.371 GHz IF. The increased mix frequency limited the Lorch filter noise rejection at the low frequency end; the total noise power increase from image noise was measured to be 0.5 dB at 0.2 GHz IF. The transfer function of the high-frequency mixing stage was directly measured and also modeled with a cascade analysis, and good agreement was found. The gain was 16 – 22 dB peaked at 0.4 GHz IF; the modest gain falloff is due at low frequency to the Lorch filter response and at high frequency to the amplifier gain response.

The coupled output of the primary IF band was connected to a Tektronix RSA5106B Real-Time Signal Analyzer. The RSA served as the primary data acquisition device during system commissioning owing to its wider tunable signal frequency bandwidth and dynamic range. This parallel signal pathway also allowed a system comparison with the Phase I benchmark (see figure 11). Differences between the internal filters and amplification of the RSA and ROACH signal paths (see figure 13) give rise to variations in the observed frequency dependence of noise between the two systems.

The ROACH-2 digitizer [42], which was integrated into a more flexible data acquisition system [43], served as the production digitizer for all Phase II physics data [37]. The ROACH FPGA was clocked at 1.6 GHz by a signal from a Hewlett-Packard 8648D signal generator. The ROACH uses an 8-bit EV8AQ160 quad ADC chip, which digitizes interleaved at 3.2 GS/s for a Nyquist frequency of 1.6 GHz. The ROACH input was directly digitized, requiring a conditioning stage to appropriately match the input.

The high-frequency mixing stage outputs were connected by long cables to the ROACH conditioning stage (see figure 15). The signal was first low-pass filtered with a MiniCircuits SLP-1650+ to remove frequencies above Nyquist. A combination fixed amplifier and MiniCircuits ZX76-31-SP-S+ attenuator provided tunable gain for this stage, so that the input signal to the ROACH was optimized for its dynamic range [44]. The signal was then passed through a directional coupler, with the coupled output monitored by MiniCircuits ZX47-50LN-S+ power meters. The mainline coupler output was the stage output, which was connected by a short cable to the ROACH input.

A Raspberry Pi (RPi) microcontroller in the ROACH conditioning stage allowed control and monitoring of the conditioning stage functionality. Two single-pole double-throw switches controlled the input source, which was manipulated by the RPi GPIO pins: both the primary and secondary IF bands from the high frequency mixing stage were connected to the stage. Additionally, a noise source for calibration of the ROACH was permanently installed and a test tone input was available on the front panel. The attenuator was controlled by SPI interface, providing 30 dB of tunable range

2026 JINST 21 P02026

in discrete sub-dB steps. One power meter was connected to an Adafruit ADS1115 ADC board, which was regularly read out by the RPi by I^2C interface. Prior to any datataking, the power level was verified and the attenuator level adjusted as necessary.

The performance of the ROACH conditioning stage was verified with measurements prior to installation. The transfer function was measured to be smooth across the signal bandwidth, falling by 5 dB over the entire range. The image noise was controlled by the low-pass filter, with the noise power increase limited at the high frequency end to <0.5 dB by 1.4 GHz. This is the more significant image noise contribution for the Phase II analyses, as this noise falls in the tritium analysis window at the low-energy side, and this filter response is less sharp than the Lorch filter of the high-frequency stage resulting in a wider impacted frequency range. These characterization measurements also calibrated the power meter response and verified isolation between all input channels.

To guarantee the optimal performance of this complex RF system, a Y-factor method was employed to assess the receiver system's RF background and gain characteristics. This involved changing the terminator temperature and analyzing its effect on the power spectrum using a thermodynamic model. The results of this analysis are shown in figure 16, which illustrates the system gain varying between 69 dB and 82 dB across the frequency interval from 24.5 GHz to 26.1 GHz. The noise temperature was determined to be ~ 132 K, driven primarily by thermal noise from the terminator. A detailed discussion of this analysis is presented in Appx. A. The frequency-dependence of the RF properties of the system was considered in the final analysis through an extensive electron-data-driven study of how the electron detection efficiency varied with frequency [32].

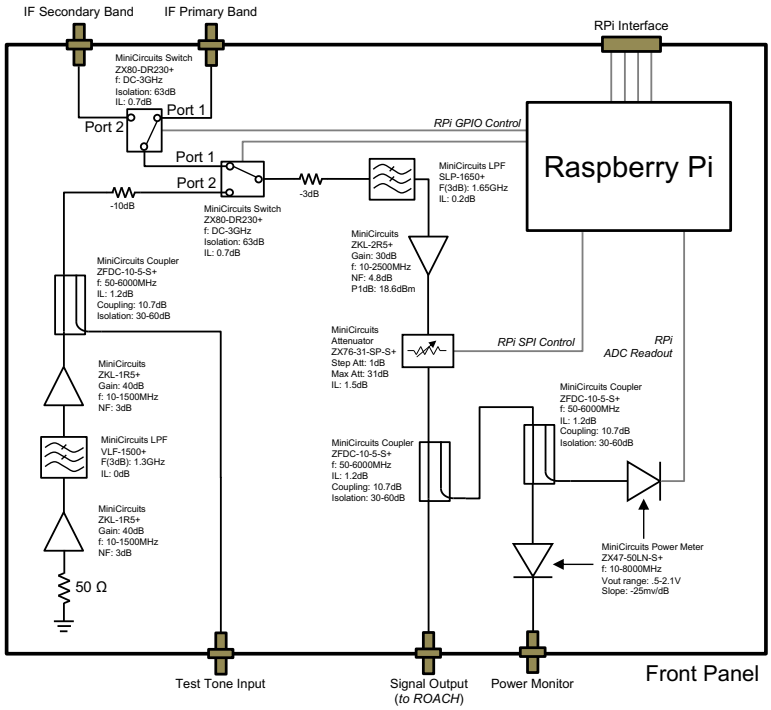

Figure 15. The Phase II ROACH conditioning stage. IF CRES signals from the high-frequency mixing stage were low-pass filtered and amplified to optimally match the ROACH-2 digitizer system. An integrated Raspberry Pi controlled the ROACH input source and attenuation level, as well as regularly monitored the power level output to the ROACH.

2026 JINST 21 P02026

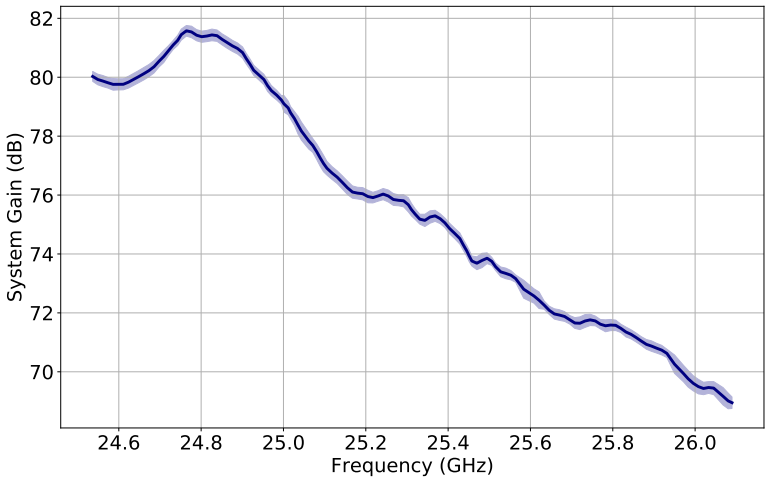

Figure 16. System gain as a function of frequency as determined using the Y-factor method. Derived from measurements taken with the ROACH-2 and the full production RF chain.

5 Gas system

The gas system was designed to operate in two configurations: 1) supplying the CRES cell with a controllable pressure of T_2 gas for performing the study of molecular tritium beta decay; and 2) supplying ^{83m}Kr, which emits monoenergetic conversion electrons at several energies between 7 keV and 32 keV. The known-energy electrons from ^{83m}Kr were used to measure the magnetic field via eq. (1.2) [32, 45], and the K-line electrons at 17.824 keV [46], close to the tritium endpoint energy of 18.574 keV, were used to characterize detector response and detection efficiency [32] in this region.

Control of the gas environment was a major consideration in the design of this system. It was necessary to tune the T_2 density to maximize the event rate by balancing the rate of decays in the apparatus (driving optimal density higher) with efficient detection (driving optimal density lower).[3] To enable accurate calibration, the ^{83m}Kr data needed to be taken in an environment tuned to be as similar as possible to the conditions during tritium running. Because electron-gas collisions are what cause CRES tracks to end, and track length is strongly tied to efficiency, matching this collision rate was particularly important. The ^{83m}Kr gas source did not produce enough gas on its own, so an inert gas needed to be mixed in with the ^{83m}Kr gas during calibration data-taking to increase the collision rate. H_2 gas was a convenient choice because of the shared infrastructure with T_2 handling and a similar scattering tail distortion to the line shape [32] due to the matched ionization energy. In both running configurations, getter pumps were used to irreversibly remove contaminants while reversibly storing and controlling the pressure of the relevant hydrogen isotope: T_2 for tritium operation, and H_2 for ^{83m}Kr operation. The pressure of the hydrogen isotope was adjusted

[3] While a higher gas density would have increased the number of decays, it also would have resulted in more frequent collisions between the electron and the gas molecules. This would have reduced the mean time during which electrons could cyclotron-radiate before the first collision, making the signal more difficult to detect [28, 47, 48]. Even if later parts of the signal could be detected, missing the first portion of the signal would have caused a systematic shift in the measured start energy toward lower values, requiring a correction in the analysis phase [32].

2026 JINST 21 P02026

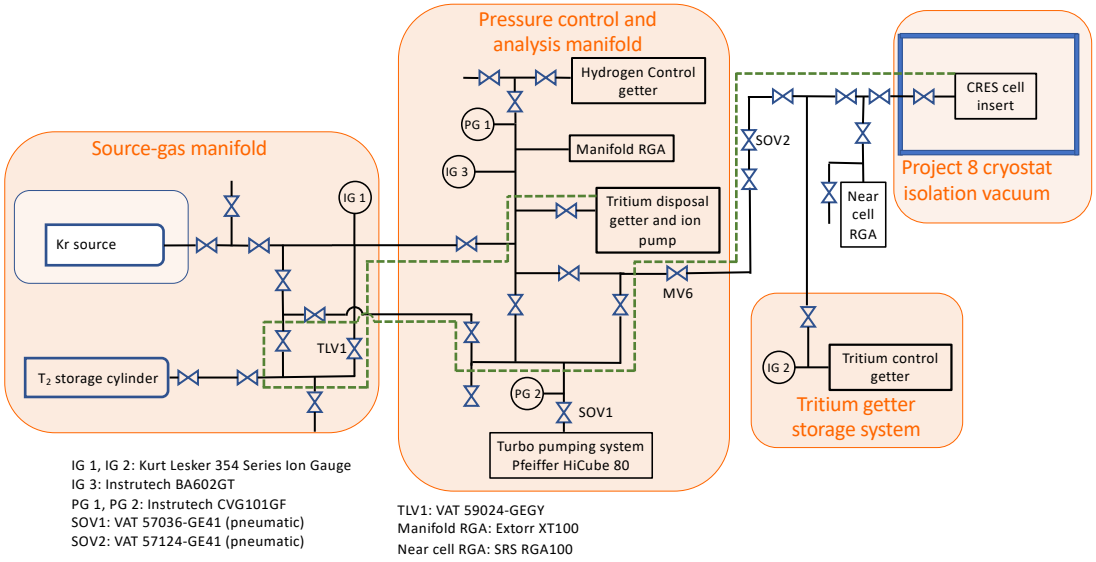

Figure 17. Gas system diagram for the combined Kr/T_2 gas system. The dashed green line shows the path used for pumping ^{3}He during T_2 data-taking.

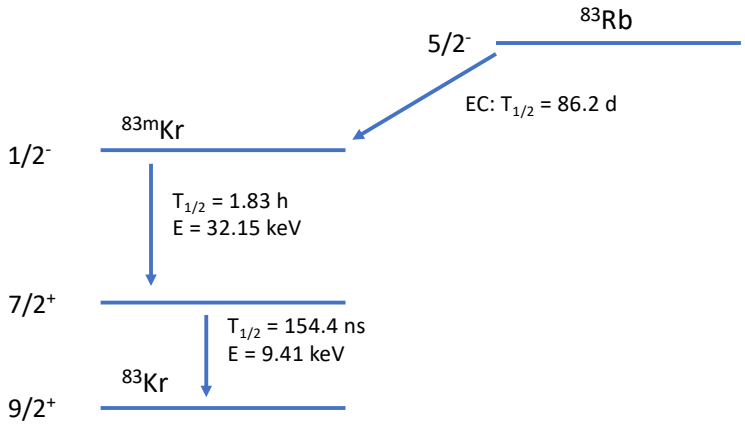

Figure 18. Decay scheme of ^{83}Rb. ^{83}Rb decays to ^{83m}Kr through an electron capture process. ^{83m}Kr decays to its ground state in a cascade of two internal conversion processes, emitting electrons.

by controlling the appropriate getter's temperature. Figure 17 shows the valve schematics for the combined Kr/T_2 gas system, which has three distinct sections: the source-gas manifold, the pressure control and analysis manifold, and the tritium getter storage system.

The sources of radioactive gases were attached to the source-gas manifold. The ^{83m}Kr source consisted of ^{83}RbCl adsorbed on Zeolite beads (2 mm in diameter) encased in lead shielding. ^{83m}Kr was formed as the decay product of ^{83}Rb (figure 18). As a noble gas, ^{83m}Kr was not retained in the zeolite matrix and it diffused into the main gas system [49]. Two ^{83}Rb sources with activities of 8 mCi and 6 mCi, installed in July 2018 and July 2019 respectively, were used for the majority of the calibration studies.

A stainless steel Swagelok SS-4CS-TW-50 cylinder was used to store 2 Ci of T_2 gas from American Radiolabeled Chemicals (figure 19). Two Swagelok SS-4-BG-TW VCR all-metal valves

2026 JINST 21 P02026

Figure 19. The tritium storage cylinder.

were welded to the cylinder with a small volume enclosed between them to allow for a controlled release of the gas into the system by successive opening and closing. To further control the release of tritium gas into the system, a digitally-controlled VAT 59024-GEGY leak valve (TLV1 in figure 17) was included in the source-gas manifold.

The pressure control and analysis manifold contained the measurement devices and pumps. Two Instrutech CVG101 convection gauges measured pressures in the range of 1×10^{-4} to 1 torr. An Instrutech BA602 ion gauge measured low pressures down to 4×10^{-10} torr. The gas composition was assessed using an ExTorr XT100 residual gas analyzer (referred to as the 'manifold RGA' from this point forward).

The main turbopump, a Pfeiffer HiCube 80, was connected to the system via a VAT 57036-GE41 solenoid valve (SOV1 in figure 17), which automatically shut during power fluctuations to prevent radioactive gas leakage into the laboratory. Base pressures of $\sim 10^{-9}$ torr were obtained using the HiCube pump after the system's bake-out. To monitor for tritium leaks, radioactive contamination surveys using swipes assayed with a liquid scintillation counter were done weekly from multiple locations on the gas system. The system was also monitored for leaks by performing regular automated scans with the RGA to detect any incursion of atmospheric gases (e.g., argon).

In addition to the mechanical turbomolecular pump, two non-evaporable getters were included in this manifold. An SAES NEXTorr D 100-5 NEG pumping system contained the disposal getter, which was used to reduce the tritium partial pressure in the system to a negligible level before ^{83m}Kr calibration runs and after the completion of data-taking with tritium (Tbl. 1). The integrated diode pump made it possible to also remove noble gases that could not be pumped by the getter.

A SAES GP-50 non-evaporable getter pump (hydrogen control getter) was used to control the density of hydrogen gas during ^{83m}Kr measurements to match the scattering rate under tritium running conditions (Tbl. 1). The pressure in the gas system was an easily measurable proxy that correlated well to the electron scattering rate in the CRES cell, so it was used as the process variable. [4] The

[4]It was an imperfect but still usable proxy, in the following ways. 1) The gas pressure and density in the cold cell and at the warm ion gauge were not the same, but were monotonically related in a time-stable way. Also, 2) the ion-gauge-measured

2026 JINST 21 P02026

Table 1. Getter pumps used in the gas system and their functions.

Getter name	Manufacturer & model number	Function
Hydrogen control getter	SAES GP-50	Raising the gas pressure for the ^{83m}Kr runs by introducing hydrogen into the system in order to reproduce the tritium run conditions.
Disposal getter	SAES NEXTorr D 100-5 NEG	Maintaining low background pressures for the ^{83m}Kr runs after the system was tritiated and absorbing the tritium after the conclusion of the tritium runs.
Tritium control getter	SAES St-172	Regulating the tritium pressure and pumping the background gases in the CRES cell during tritium runs.

target pressure was settable over a range of several orders of magnitude and maintained by an Omega CN16DPt PID controller unit which adjusted the electrical current supplied to the activation filament in the non-evaporable getter pump.

Similarly, the tritium getter storage system was designed to regulate the tritium gas pressure in the CRES cell. This system contained a SAES St-172 zirconium-based non-evaporable getter (referred to as the tritium control getter from this point forward) that was loaded with molecular tritium. A dedicated Omega CN16DPt PID controller regulated the pressure of tritium inside the CRES cell by temperature-controlling the tritium control getter. This getter also pumped background gases in the CRES cell (Tbl. 1).

The tritium control getter was installed in a mini-conflat half nipple. Around the half nipple a copper tube was brazed, through which cooling water was flowed while the getter was running at high temperatures. The delicate filament connectors of the getter were crimped into two small copper tubes which were connected to a vacuum feed-through. A C-type thermocouple was mounted inside the annular storage getter for measuring its temperature. The thermocouple connectors were electrically isolated with ceramic beads. Figure 20 shows this setup before the final assembly. A Kurt J. Lesker (KJL) 354 series ion gauge was used to monitor the pressure in the tritium getter storage system, providing the reference signal for the PID pressure controller. When not taking tritium data, the tritium was confined to the tritium storage getter region by closing a manual valve. The tritium getter storage system was connected to the rest of the gas system via a shut-off valve (SOV2 in figure 17); this valve would automatically close to limit the tritium-exposed volume in case of a power outage. A Stanford Research Systems RGA100 residual gas analyzer (referred to as the 'near-cell RGA' from this point forward) was installed as close as possible to the CRES cell to assess gas composition during tritium data-taking (figure 17).

The gas-pressure-control system worked as intended in both ^{83m}Kr calibration and tritium running modes. Pressures in the range 1.2 to 2.0 µtorr were used for the main data sets[5], with ±3% stability

pressure and electron scattering rate depend differently on gas composition, making it necessary to measure their relationship separately for the T_2 data and the ^{83m}Kr data; however, this was done successfully and pressures were set that closely matched the electron scattering rates in the two run modes [32].

[5]The ion gauges were set to H_2-equivalent, so the pressures are different for ^{83m}Kr and tritium data to account for the ion

2026 JINST 21 P02026

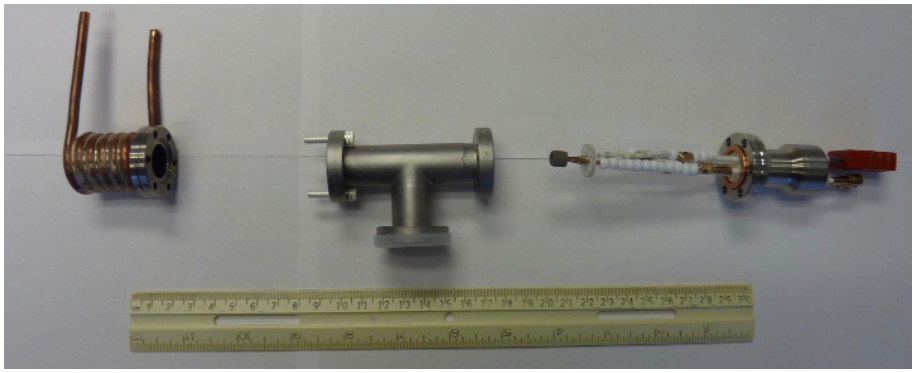

Figure 20. Tritium getter storage system components before their final assembly.

run-to-run. With this system in place, CRES data were acquired in ^{83m}Kr calibration mode at a range of pressures to characterize the dependence of detection efficiency on gas pressure. As described in ref. [32], this information was used to inform the choice of set pressure for the tritium data run to maximize event rate.

5.1 T_2 data-taking

To test the storage-getter-based density control mechanism without the radioactivity-associated safety concerns of working with tritium, tests using deuterium were performed first. The relation between the equilibrium pressure of hydrogen isotopes and the getter temperature was examined. The results of these tests are described in detail in Appx. B.

After the conclusion of the deuterium tests, the tritium cylinder was installed. The tritium was absorbed into the tritium control getter, after which ^{3}He (the product of tritium decays that had occurred before installation) was removed with the ion pump.

One challenge in maintaining high tritium purity in the CRES cell was the presence of ^{3}He, which came from two sources. 1) The tritium adsorbed on the stainless-steel walls of the getter compartment during the tritium fill released ^{3}He into the system. This source was suppressed by baking the getter compartment for several hours, which drove the tritium into the tritium control getter. 2) ^{3}He was also produced in tritium decay inside the tritium control getter, where it was not all trapped. After the impact of this effect was discovered, the gas system was modified to establish a path for continuous pumping by the ion pump (figure 17). The gas flow through the leak valve was tuned to efficiently remove ^{3}He from the gas system without excessive loss of the T_2 inventory in the tritium control getter. The manifold RGA, which was placed close to the ion pump, was used to estimate an upper limit of a tritium pumping rate of 34 mCi/yr. Figure 21 compares the gas composition measured by the two residual gas analyzers during the tritium data campaign confirming that the continuous pumping worked as expected. The near-cell RGA's spectrum was dominated by mass 2, 4, and 6, corresponding to H_2, HT, and T_2. This demonstrated the presence of high partial pressures of hydrogen isotopes in the CRES cell. Smaller amounts of ^{3}He and CO (mass 3 and 28) were also apparent as the major background gases. The ^{3}He was more prominent in the manifold RGA's spectrum both because the conductance of the leak valve (TLV1) was higher for this light isotope, and because it was only removed by the ion pumping. A quantitative analysis of the gas composition in running conditions, based on residual

gauge's different sensitivity to hydrogen isotopes and Kr.

2026 JINST 21 P02026

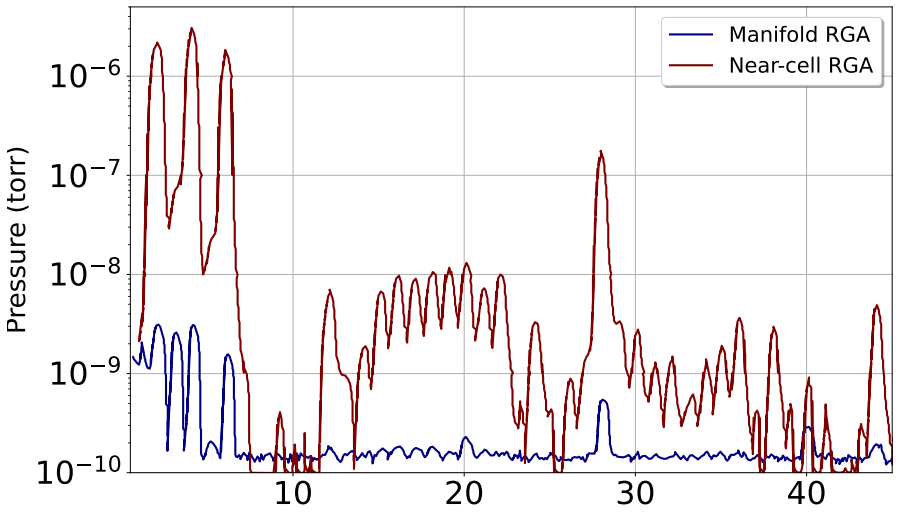

Figure 21. The gas composition measured by the manifold RGA (blue) and the near-cell RGA (red) during tritium data taking. The two spectra are approximate measures of the partial pressures in the ion pump and in the CRES cell.

gas analyzer data, is described in [32]. In brief, it was found that 91±5% of scattering events during tritium data-taking were from hydrogen isotopes, demonstrating the gas system's good performance.

6 Conclusion

In this work we have described the apparatus used in Phase II of the Project 8 experiment and shown how hardware improvements over Phase I made it possible to set the first frequency-based neutrino mass limit [14, 32].

The new gas system for Phase II was the first to deliver tritium to a CRES apparatus. Its pressure-controlled delivery of multiple gas species also made it possible to take ^{83m}Kr calibration data in similar conditions to tritium data, characterizing detector response in great detail and enabling improved and better-understood resolution. A new field-shifting solenoid enabled us to also map the frequency variation of detection efficiency using ^{83m}Kr data. These tools were crucial for gathering the calibration data needed for the fit to the tritium endpoint.

In addition to incorporating tools to characterize systematic effects and noise, the Phase II apparatus was also built to suppress them. An RF-absorbing terminator suppressed strong frequency dependence in the signal gain, greatly simplifying signal morphology and reducing the variation of detector response with frequency. While the RF terminator nominally sacrificed signal amplitude at some frequencies, this was compensated for by using a circular rather than a rectangular waveguide enabling the collection of both polarizations of upward-propagating radiation. A thermal break allowed the cryogenic amplifiers to be colder, and a circulator suppressed noise emitted backward from the input of the amplifier; both of these reduced noise. Despite the additional noise from the terminator, these advances together lowered the overall noise temperature from Phase I to Phase II. The net effect of all these changes was an improved and more consistent signal-to-noise ratio.

2026 JINST 21 P02026

Phase II also enabled improvements in electron trapping that led to both higher event rates and better resolution. Its circular waveguide has a larger trap volume than Phase I's rectangular waveguide. Phase II's multiple harmonic traps could be characterized and tuned precisely to enable high resolution even in the presence on an imperfectly homogeneous background magnetic field. They were also able to be deepened and used simultaneously to optimize for larger trapping volume and high event rate, an important tool for increasing sensitivity for the statistics-limited tritium measurement.

The overarching goal of the Phase II design—to create an apparatus whose signal could be fully understood and all systematics quantitatively characterized—was achieved. The lessons learned from the Phase II hardware also have built the foundations for future CRES experiments, including prompting an exploration into resonant-cavity-based detectors, which promise frequency-dependent but characterizable detection efficiency and increased signal power due to enhanced spontaneous emission.

Acknowledgments

This material is based upon work supported by the following sources: the U.S. Department of Energy Office of Science, Office of Nuclear Physics, under Award No. DE-SC0020433 to Case Western Reserve University (CWRU), under Award No. DE-SC0011091 to the Massachusetts Institute of Technology (MIT), under the Early Career Research Program to Pacific Northwest National Laboratory (PNNL), a multiprogram national laboratory operated by Battelle for the U.S. Department of Energy under Contract No. DE-AC05-76RL01830, under Early Career Award No. DE-SC0019088 to Pennsylvania State University, under Award No. DE-FG02-97ER41020 to the University of Washington, and under Award No. DE-SC0012654 to Yale University; the National Science Foundation under Grant No. PHY-2209530 to Indiana University, and under Grant No. PHY-2110569 to MIT; the Cluster of Excellence "Precision Physics, Fundamental Interactions, and Structure of Matter" (PRISMA+ EXC 2118/1) funded by the German Research Foundation (DFG) within the German Excellence Strategy (Project ID 39083149); the Karlsruhe Institute of Technology (KIT) Center Elementary Particle and Astroparticle Physics (KCETA); the MIT Wade Fellowship; the LDRD Program at PNNL; the University of Washington Royalty Research Foundation; and Yale University. A portion of the research was performed using Research Computing at PNNL. The isotope(s) used in this research were supplied by the United States Department of Energy Office of Science by the Isotope Program in the Office of Nuclear Physics.

A Investigation of the RF noise background

In this section, we present an analysis of the noise and gain of the receiver chain of Phase II. To this end, the terminator temperature was altered and its effect on the power spectrum was analyzed using a thermodynamic model.

The RF background was determined from the power spectral density (PSD) when no electrons were trapped in the cell. The background was measured using the ROACH-2 digitizer (as opposed to the phase comparison measurement with the RSA, figure 11) with a frequency span of 24.5 GHz to 26.1 GHz. The spectrum was obtained from applying the Welch method to 26,214,400 time samples [50].

The RF background was measured as a function of cell temperature from 58 K to 110 K. The cell and amplifier temperatures were monitored using calibrated Lakeshore Cernox-87821 temperature sensors. Other temperatures along the cryogenic insert were measured with PT100 sensors.

2026 JINST 21 P02026

A thermodynamic model was developed to describe the RF background as the sum of the black-body radiation of each mechanical component of the cryogenic insert and the Johnson noise of each electronic component. Recall that in the high-temperature regime, the black-body radiation is $P_n/B = k_B T$, where P_n is the noise power, B is the total bandwidth over which the noise is measured, k_B is the Boltzmann constant, and T is the temperature. For the noise contribution of electronic components, the Johnson noise is expressed in the same form using an equivalent noise temperature T_n. From the measured noise power, an equivalent system noise temperature, T_{sys}, is defined,

$$P_n = T_{sys} G k_B B, \tag{A.1}$$

where G is the total system gain.

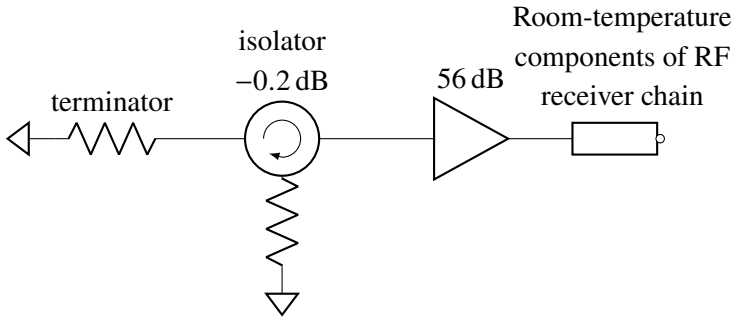

Figure 22. Thermal model for the noise power of the cryogenic insert. The black-body radiation from the terminator traveled up the waveguide, through the isolator, and into the first-stage amplifier. The isolator absorbed some of the terminator's radiation and re-emitted it as its own black-body radiation.

The thermodynamic model in figure 22 is developed to describe the noise power in Phase II. The fraction of thermal photons from the terminator that reaches the amplifier is η_{iso}, the isolator's transmissivity. The isolator absorbs a fraction $(1 - \eta_{iso})$ of photons and emits blackbody radiation $P/B = \epsilon_{iso} k_B T_{iso}$, where T_{iso} and ϵ_{iso} are the isolator's temperature and emissivity. By Kirchoff's law, the isolator's emissivity is equal to the fraction of the blackbody radiation that the isolator absorbs, $\epsilon_{iso} = 1 - \eta_{iso}$. The amplifier adds to the signal its Johnson noise, which is written as an equivalent noise temperature T_{amp}.

The noise contribution from the next components of the receiver system is negligible except for the contribution from digitization noise and image noise. Hence, T_{amp} is considered to be the equivalent noise temperature of the receiver, from the first-stage amplifier to the digitizer.

The resulting noise temperature from the thermodynamic model is

$$T_{sys} = T_{term}\eta_{iso} + T_{iso}(1 - \eta_{iso}) + T_{amp}. \tag{A.2}$$

The isolator temperature T_{iso} depends linearly on T_{term} and is written as $T_{iso} = aT_{term} + b$. Sensor data were used to extract the parameters a and b (figure 23). T_{sys} is written as a linear function of T_{term}, T_{sys}, and the RF background is modeled as

$$\begin{aligned} P_n = GBk_B([\eta_{iso} + a(1 - \eta_{iso})]T_{term} \\ + b(1 - \eta_{iso}) + T_{amp}) \end{aligned} \tag{A.3}$$

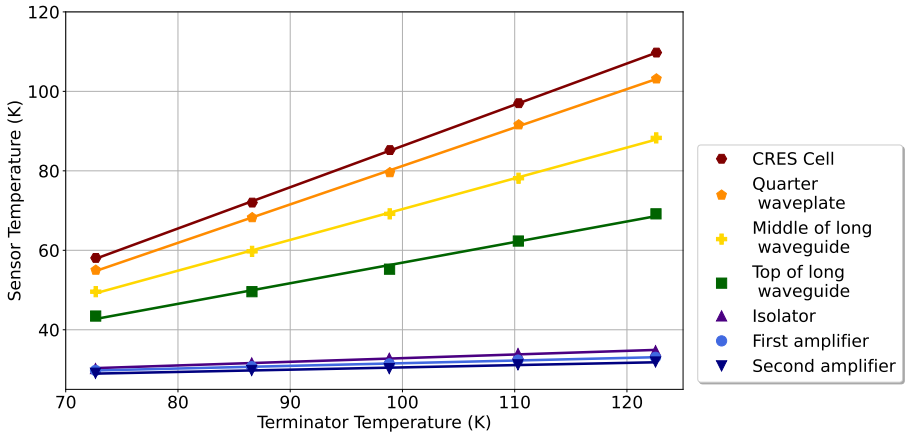

Figure 23. Temperature along the cryogenic insert as a function of terminator temperature with linear fits. The plot proves the linear dependence of the temperatures along the cryogenic insert on the terminator temperature. The plot also demonstrates the effectiveness of the thermal break in maintaining low temperatures for the isolator and the amplifiers.

and the linear dependence on T_{term} is made explicit. Isolator transmissivity $\eta_{\text{iso}} = 0.955 \pm 0.045$ is used for the isolator transparency and its considerable uncertainty.

The rectangular waveguide and CRES cell are treated as lossless components in this model. However, the effect of the quarter-wave plate is non-negligible. With the inclusion of the quarter-wave plate in the thermal model, eq. (A.2) is modified to

$$\begin{aligned} T_{\text{sys}} = {} & T_{\text{term}}\eta_{\text{qwp}}\eta_{\text{iso}} + T_{\text{qwp}}(1-\eta_{\text{qwp}})\eta_{\text{iso}} \\ & + T_{\text{iso}}(1-\eta_{\text{iso}}) + T_{\text{amp}}, \end{aligned} \tag{A.4}$$

where T_{qwp} (η_{qwp}) is the temperature (transparency) of the quarter-wave plate. Assuming that the quarter-wave plate temperature was close enough to the terminator temperature, eq. (A.4) should only be more accurate than eq. (A.2) by a few percent. The model uncertainty is estimated to be 4% by taking the thermal photon's temperature as a weighted average of the terminator and quarter-wave plate and assuming 1 dB insertion loss for the quarter-wave plate.

The amplifier noise and gain were fitted from measurements of the RF background at various terminator temperatures. From the linear relationship in eq. (A.3), the terminator temperature, x_{int}, that resulted in zero noise power, $P_n = 0$, was determined regardless of the complicated frequency-dependent gain. The amplifier noise temperature was deduced, where

$$\begin{aligned} T_{\text{amp}} = {} & -[\eta_{\text{iso}} + a(1-\eta_{\text{iso}})]x_{\text{int}} \\ & - b(1-\eta_{\text{iso}}). \end{aligned} \tag{A.5}$$

The gain was evaluated from the slope of the line-fit m,

$$G = \frac{m}{Bk_{\text{B}}} \frac{1}{\eta_{\text{iso}} + a\,(1-\eta_{\text{iso}})}. \tag{A.6}$$

The calculated amplifier noise temperature was used to find the system noise temperature for a given terminator temperature using eq. (A.2).

2026 JINST 21 P02026

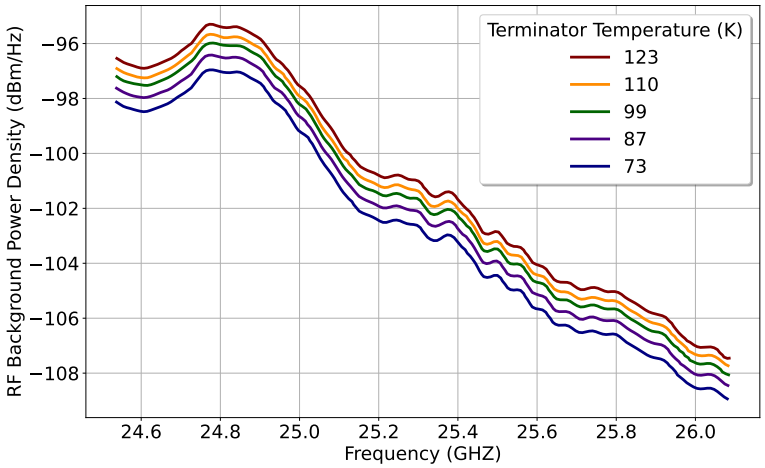

Figure 24. RF background power spectral density as a function of frequency and terminator temperature.

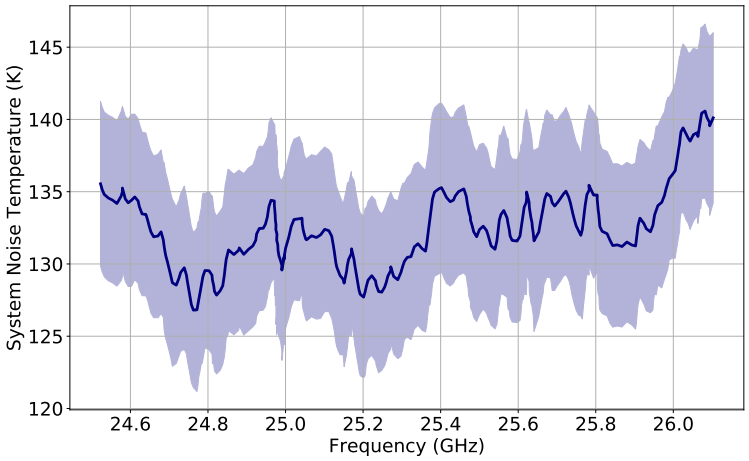

Figure 25. System noise temperature obtained from the Y-factor method when the terminator was at 99 K and the cell was at 85 K.

Figure 24 shows the RF background as a function of terminator temperature. The system noise temperature was calculated when operating the CRES cell at 85 K (figure 25). The system noise temperature was estimated to be 132 K with a 5% uncertainty.

Finally, the system gain was determined by using eq. (A.6) (see figure 16). The gain ranged from 82 dB to 69 dB with an average uncertainty (in the logarithmic scale) of about 0.3%.

B D_2 tests

Tests using deuterium were performed to investigate the performance of the storage getter without the safety concerns associated with tritium operation. One of the objectives for these tests was to examine the relation between the equilibrium pressure and the getter temperature to ensure the proper

2026 JINST 21 P02026

functionality of the tritium control getter. For hydrogen isotopes in a metallic getter, the equilibrium pressure P (in torr) can be derived from Sievert's law, in which

$$\log P = a + 2\log q - \frac{b}{T}, \tag{B.1}$$

where q is the hydrogen concentration in the metallic alloy (in $\mathrm{L}\cdot\mathrm{torr/g}$), T is the temperature (in K), and a and b are constants that must be measured for each getter individually. According to this equation, the equilibrium pressure increases with the getter's temperature and hydrogen concentration.

The tritium control getter was loaded with deuterium at its operating temperature of 400 °C until an equilibrium pressure of 2.2 µtorr was achieved. Next, the tritium control getter was cooled down to room temperature and then the filament's current was incremented in 0.5 A steps. The partial pressures of hydrogen isotopes measured with the residual gas analyzer are plotted in figure 26. The main gas component was D_2 with smaller partial pressures of HD and H_2 present in the system. Although a C-type thermocouple was mounted touching the interior surface of the annular getter, its thermal coupling to the surface of the getter was unknown. The temperature was therefore monitored by tracking the resistance of the molybdenum filament inside the getter instead.

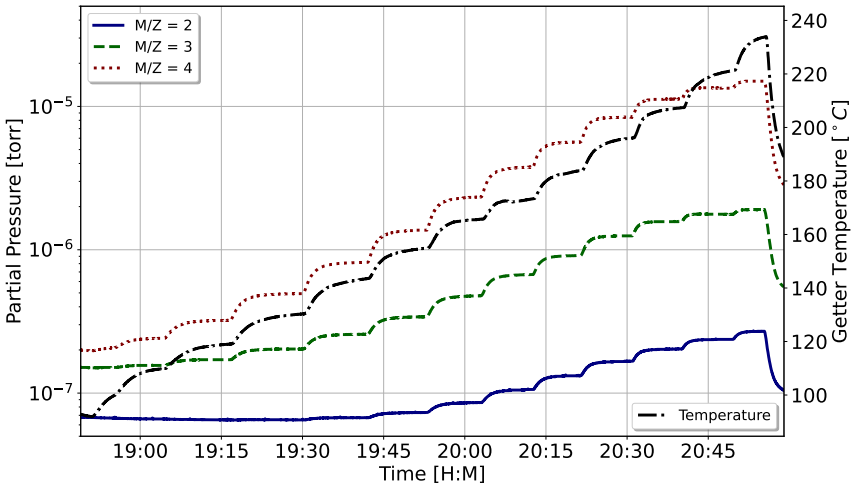

Figure 26. Measured partial pressures of hydrogen isotopes with time as the getter temperature (black) was changed.

The ion gauge measurement was used to find the equilibrium pressure for each step with a given current. Note that the residual gas analyzer data could only be used for relative pressure measurement due to the unknown normalization factor.

Figure 27 shows the equilibrium pressure in the system as a function of the getter temperature. The data were fitted with Sievert's law, eq. (B.1), to deduce the empirical coefficients. According to the SAES St 172 getter manual, the value for the temperature coefficient (b in eq. (B.1)) is 5730 K which is in agreement with our extracted value of 5712(43) K. The total amount of deuterium in the getter was also estimated to be 4.4(5) torr L using the fit in figure 27, eq. (B.1), the getter mass (550 mg), the value of $a = 4.45$ for hydrogen from the manual [51], and the fact that the equilibrium pressure of a hydrogen isotope is inversely proportional to the square root of the atomic mass number [52].

2026 JINST 21 P02026

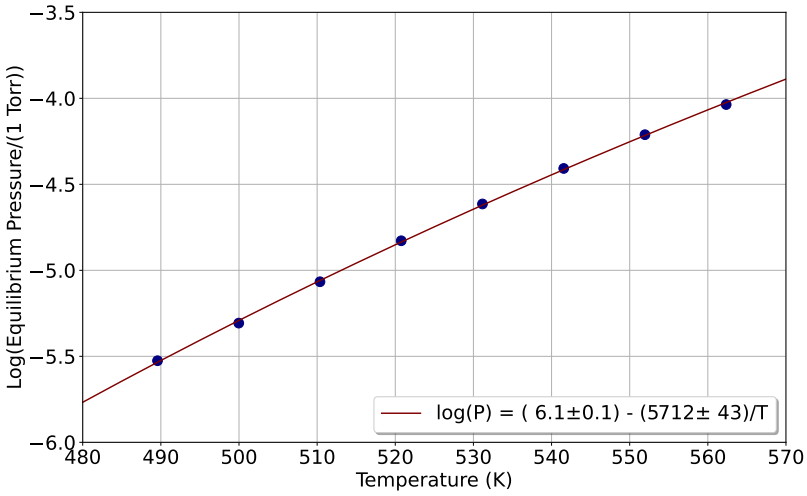

Figure 27. The measured equilibrium pressure vs. temperature for eight different values of the getter's filament current. The data were fitted with the Sievert's law equation (eq. (B.1)).

References

[1] Super-Kamiokande collaboration, *Evidence for oscillation of atmospheric neutrinos*, *Phys. Rev. Lett.* **81** (1998) 1562 [hep-ex/9807003].

[2] SNO collaboration, *Direct evidence for neutrino flavor transformation from neutral current interactions in the Sudbury Neutrino Observatory*, *Phys. Rev. Lett.* **89** (2002) 011301 [nucl-ex/0204008].

[3] Particle Data Group collaboration, *Review of particle physics*, *Phys. Rev. D* **110** (2024) 030001.

[4] KamLAND-Zen collaboration, *Search for Majorana Neutrinos with the Complete KamLAND-Zen Dataset*, arXiv:2406.11438.

[5] LEGEND collaboration, *First Results on the Search for Lepton Number Violating Neutrinoless Double Beta Decay with the LEGEND-200 Experiment*, arXiv:2505.10440.

[6] GERDA collaboration, *Final Results of GERDA on the Search for Neutrinoless Double-β Decay*, *Phys. Rev. Lett.* **125** (2020) 252502 [arXiv:2009.06079].

[7] Majorana collaboration, *Final Result of the Majorana Demonstrator's Search for Neutrinoless Double-β Decay in Ge76*, *Phys. Rev. Lett.* **130** (2023) 062501 [arXiv:2207.07638].

[8] EXO-200 collaboration, *Search for Neutrinoless Double-β Decay with the Complete EXO-200 Dataset*, *Phys. Rev. Lett.* **123** (2019) 161802 [arXiv:1906.02723].

[9] CUORE collaboration, *Search for Majorana neutrinos exploiting millikelvin cryogenics with CUORE*, *Nature* **604** (2022) 53 [arXiv:2104.06906].

[10] Planck collaboration, *Planck 2018 results. VI. Cosmological parameters*, *Astron. Astrophys.* **641** (2020) A6 [*Erratum ibid.* **652** (2021) C4] [arXiv:1807.06209].

[11] eBOSS collaboration, *Completed SDSS-IV extended Baryon Oscillation Spectroscopic Survey: Cosmological implications from two decades of spectroscopic surveys at the Apache Point Observatory*, *Phys. Rev. D* **103** (2021) 083533 [arXiv:2007.08991].

2026 JINST 21 P02026

[12] DESI collaboration, *Constraints on Neutrino Physics from DESI DR2 BAO and DR1 Full Shape*, arXiv:2503.14744.

[13] KATRIN collaboration, *Direct neutrino-mass measurement based on 259 days of KATRIN data*, *Science* **388** (2025) adq9592 [arXiv:2406.13516].

[14] Project 8 collaboration, *Tritium Beta Spectrum Measurement and Neutrino Mass Limit from Cyclotron Radiation Emission Spectroscopy*, *Phys. Rev. Lett.* **131** (2023) 102502 [arXiv:2212.05048].

[15] L. Gastaldo et al., *The electron capture in^{163}Ho experiment — ECHo*, *Eur. Phys. J. ST* **226** (2017) 1623.

[16] B.K. Alpert et al., *Most stringent bound on electron neutrino mass obtained with a scalable low temperature microcalorimeter array*, arXiv:2503.19920.

[17] G. Drexlin, V. Hannen, S. Mertens and C. Weinheimer, *Current direct neutrino mass experiments*, *Adv. High Energy Phys.* **2013** (2013) 293986 [arXiv:1307.0101].

[18] J.A. Formaggio, A.L.C. de Gouvêa and R.G.H. Robertson, *Direct Measurements of Neutrino Mass*, *Phys. Rept.* **914** (2021) 1 [arXiv:2102.00594].

[19] B. Pontecorvo, *Inverse Beta Processes and Nonconservation of Lepton Charge*, *Sov. Phys. JETP* **7** (1958) 172.

[20] Z. Maki, M. Nakagawa and S. Sakata, *Remarks on the unified model of elementary particles*, *Prog. Theor. Phys.* **28** (1962) 870.

[21] KATRIN collaboration, *KATRIN: status and prospects for the neutrino mass and beyond*, *J. Phys. G* **49** (2022) 100501 [arXiv:2203.08059].

[22] S. Schneidewind et al., *Improved treatment of the T_2 molecular final-states uncertainties for the KATRIN neutrino-mass measurement*, *Eur. Phys. J. C* **84** (2024) 494 [arXiv:2310.12634].

[23] L.I. Bodine, D.S. Parno and R.G.H. Robertson, *Assessment of molecular effects on neutrino mass measurements from tritium β decay*, *Phys. Rev. C* **91** (2015) 035505 [arXiv:1502.03497].

[24] B. Monreal and J.A. Formaggio, *Relativistic Cyclotron Radiation Detection of Tritium Decay Electrons as a New Technique for Measuring the Neutrino Mass*, *Phys. Rev. D* **80** (2009) 051301 [arXiv:0904.2860].

[25] He6-CRES collaboration, *First Observation of Cyclotron Radiation from MeV-Scale $e\pm$ following Nuclear β Decay*, *Phys. Rev. Lett.* **131** (2023) 082502 [arXiv:2209.02870].

[26] N. Buzinsky et al., *Larmor power limit for cyclotron radiation of relativistic particles in a waveguide*, *New J. Phys.* **26** (2024) 083021 [arXiv:2405.06847].

[27] K. Kazkaz and N. Woollett, *Using Cyclotron Radiation Emission for Ultra-high Resolution X-Ray Spectroscopy*, *New J. Phys.* **23** (2021) 033043 [arXiv:1911.05869].

[28] A. Ashtari Esfahani et al., *Track and event reconstruction for the project 8 experiment*, in preparation.

[29] Project 8 collaboration, *The Project 8 Neutrino Mass Experiment*, in the proceedings of the *Snowmass 2021*, Seattle, U.S.A., July 17–26 (2022) [arXiv:2203.07349].

[30] Project 8 collaboration, *Determining the neutrino mass with cyclotron radiation emission spectroscopy — Project 8*, *J. Phys. G* **44** (2017) 054004 [arXiv:1703.02037].

[31] Project 8 collaboration, *Single electron detection and spectroscopy via relativistic cyclotron radiation*, *Phys. Rev. Lett.* **114** (2015) 162501 [arXiv:1408.5362].

[32] Project 8 collaboration, *Cyclotron radiation emission spectroscopy of electrons from tritium β decay and Kr83m internal conversion*, *Phys. Rev. C* **109** (2024) 035503 [arXiv:2303.12055].

2026 JINST 21 P02026

[33] A. Ashtari Esfahani et al., *Bayesian analysis of a future β decay experiment's sensitivity to neutrino mass scale and ordering*, *Phys. Rev. C* **103** (2021) 065501 [arXiv:2012.14341].

[34] A. Ashtari Esfahani, *Constraining the Neutrino Mass Using Cyclotron Radiation Emission Spectroscopy*, Ph.D. thesis, University of Washington (2020) https://digital.lib.washington.edu/researchworks/handle/1773/46557.

[35] M. Ottiger, *Development of a NMR Magnetometry Probe Prototype for Project 8*, ETH Zurich (2018).

[36] J. Kofron, *A novel method for electron energy measurement: Cyclotron Radiation Emission Spectroscopy*, Ph.D. thesis, University of Washington (2015), https://digital.lib.washington.edu/researchworks/handle/1773/33235.

[37] C. Claessens, *Event detection in Project 8: Detection efficiency and its implications for the first tritium β-decay spectrum recorded with Cyclotron Radiation Emission Spectroscopy*, Ph.D. thesis, Mainz University, Mainz, Germany (2021) [DOI:10.25358/openscience-5701].

[38] M.V. Jacob, J. Mazierska, D. Ledenyov and J. Krupka, *Microwave characterisation of CaF2 at cryogenic temperatures using a dielectric resonator technique*, *J. Eur. Ceram. Soc.* **23** (2003) 2617.

[39] R. Kirby, Y. Touloukian, E. Taylor and T. Lee, *Thermophysical properties of matter - the TPRC data series. Volume 13. Thermal expansion - nonmetallic solids*, Tech. Rep. Purdue University (1977), https://ntrl.ntis.gov/NTRL/dashboard/searchResults/titleDetail/PB276203.xhtml.

[40] A. Ashtari Esfahani et al., *Electron Radiated Power in Cyclotron Radiation Emission Spectroscopy Experiments*, *Phys. Rev. C* **99** (2019) 055501 [arXiv:1901.02844].

[41] A. Ashtari Esfahani et al., *Cyclotron radiation emission spectroscopy signal classification with machine learning in project 8*, *New J. Phys.* **22** (2020) 033004 [arXiv:1909.08115].

[42] J. Hickish et al., *A Decade of Developing Radio-Astronomy Instrumentation using CASPER Open-Source Technology*, *J. Astron. Inst.* **05** (2016) 1641001 [arXiv:1611.01826].

[43] A. Ashtari Esfahani et al., *The real-time data processing and acquisition system for Project 8 Phase II*, *Nucl. Instrum. Meth. A* **1081** (2026) 170843 [arXiv:2506.22392].

[44] N.A. Patel et al., *CHaracterizing the performance of a high-speed ADC for the SMA digital backend*, *J. Astron. Inst.* **03** (2014) 1450001.

[45] E.W. Otten and C. Weinheimer, *Neutrino mass limit from tritium beta decay*, *Rept. Prog. Phys.* **71** (2008) 086201 [arXiv:0909.2104].

[46] D. Vénos et al., *Properties of 83mKr conversion electrons and their use in the KATRIN experiment*, 2018 *JINST* **13** T02012.

[47] A. Esfahani Ashtari et al., *Viterbi decoding of CRES signals in Project 8*, *New J. Phys.* **24** (2022) 053013 [arXiv:2112.05265].

[48] A. Ashtari Esfahani et al., *Deep learning based event reconstruction for cyclotron radiation emission spectroscopy*, *Mach. Learn. Sci. Tech.* **5** (2024) 025026 [arXiv:2402.13256].

[49] D. Vénos, A. Špalek, O. Lebeda and M. Fišer, *Kr radioactive source based on Rb trapped in cation-exchange paper or in zeolite*, *Appl. Radiat. Isot.* **63** (2005) 323.

[50] P. Welch, *The use of fast Fourier transform for the estimation of power spectra: A method based on time averaging over short, modified periodograms*, *IEEE Trans. Audio Electroacoust.* **15** (1967) 70.

[51] SAES Getters, *St 171 and St 172 - Sintered Porous Getters*, 2007.

[52] Y. Yamamoto et al., *Characteristics of Gas Mixture Supply/Pressure Control Using Non-Evaporable Getters in a Discharge-Type Fusion Neutron Source*, *Fusion Sci. Technol.* **72** (2017) 773.

2026 JINST 21 P02026